AGU100 ADVANCING EARTH AND SPACE SCIENCE

JGR

Journal of Geophysical Research: Earth Surface

RESEARCH ARTICLE
10.1029/2017JF004408

Key Points:
- Surface mass balance dominates the interannual variability in Sermilik glacier total mass balance
- South Greenland ice sheet accumulation and ablation observations reveal Sermilik glacier total mass loss being 20 times the Greenland ice sheet average
- Three RCMs underrate melt below ELA due to some combination of overestimated snowfall and ice albedo and underestimated downward turbulent heat flux

Supporting Information:
- Supporting Information S1

Correspondence to:
M. Hermann and J. Box,
hermannm@student.ethz.ch;
jeb@geus.dk

Citation:
Hermann, M., Box, J. E., Fausto, R. S., Colgan, W. T., Langen, P. L., Mottram, R., et al. (2018). Application of PROMICE Q-transect in situ accumulation and ablation measurements (2000–2017) to constrain mass balance at the southern tip of the Greenland ice sheet. *Journal of Geophysical Research: Earth Surface, 123*, 1235–1256. https://doi.org/10.1029/2017JF004408

Received 22 JUN 2017
Accepted 9 APR 2018
Accepted article online 20 APR 2018
Published online 5 JUN 2018

Application of PROMICE Q-Transect in Situ Accumulation and Ablation Measurements (2000–2017) to Constrain Mass Balance at the Southern Tip of the Greenland Ice Sheet

Mauro Hermann[1], Jason E. Box[2], Robert S. Fausto[2], William T. Colgan[2], Peter L. Langen[3], Ruth Mottram[3], Jan Wuite[4], Brice Noël[5], Michiel R. van den Broeke[5], and Dirk van As[2]

[1]Eidgenössische Technische Hochschule, Zurich, Switzerland, [2]Geological Survey of Denmark and Greenland (GEUS), Copenhagen, Denmark, [3]Danish Meteorological Institute, Copenhagen, Denmark, [4]Environmental Earth Observation IT GmbH, Innsbruck, Austria, [5]Institute for Marine and Atmospheric Research (IMAU), Utrecht University, Utrecht, Netherlands

Abstract With nine southern Greenland ice sheet ablation area locations, the Programme for Monitoring of the Greenland Ice Sheet (PROMICE) "Q-transect" is a source of snow accumulation and ice ablation data spanning 17 years (2000 to present). Snow water equivalence measurements below equilibrium line altitude enable resolving the location and magnitude of an orographic precipitation maximum. Snow depth skillfully predicts snow water equivalence in this region, for which we find no evidence of change 2001–2017. After describing observed accumulation and ablation spatiotemporal patterns, we examine surface mass balance (SMB) in 5.5-km HIRHAM5, 7.5-km Modèle Atmosphèrique Régional (MAR) v3.7, and 1-km Regional Atmospheric Climate Model (RACMO2.3p2) regional climate model (RCM) output. HIRHAM5 and RACMO2.3p2 overestimate accumulation below equilibrium line altitude by 2 times. MAR SMB is closer to observations but lacks a distinct orographic peak. RCM ablation underestimation is attributable to overestimated snowfall (HIRHAM5 and RACMO2.3p2), overestimated bare ice albedo (MAR), and underestimation of downward turbulent heat fluxes. Calibrated ablation area RCM SMB data yield -0.3 ± 0.5 Gt/a SMB of the 559-km^2 marine-terminating Sermilik glacier (September 2000 to October 2012). Using Enderlin et al. (2014, https://doi.org/10.1002/2013GL059010) ice discharge data, Sermilik glacier's total mass balance is -1.3 ± 0.5 Gt/a with interannual variability dominated by SMB. The area specific mass loss is 17 to 20 times greater than the whole ice sheet mass loss after Andersen et al. (2015, https://doi.org/10.1016/j.epsl.2014.10.015) and Colgan et al. (2015, https://doi.org/10.1016/j.rse.2015.06.016), highlighting the Q-transect's situation in an ice mass loss hot spot.

1. Introduction

The Greenland ice sheet has been losing mass in recent decades (Kjeldsen et al., 2015). The mass loss increased after a near balance state in the 1970/1980s to 97 ± 47 Gt/a in the 1990s, reaching 267 ± 38 Gt/a in 2007 (Rignot et al., 2008). Between 2007 and 2011, Andersen et al. (2015) found ice loss of 262 ± 21 Gt/a equivalent with 0.73 mm/a global sea level rise.

Rising Greenland air temperature since the 1980s has increased surface melt (Box & Colgan, 2013) with year 2007, 2010, and 2012 ice sheet melt extents setting new records (Tedesco et al., 2013). On the Qagssimiut ice lobe near the southern tip of the ice sheet, the largest ice melt rates observed in Greenland are shown by automated ground stations (Fausto, van As, Box, Colgan, Langen, & Mottram, 2016; Van As et al., 2013) and by survey stakes that we here name the "Q-transect" (Figure 1). In 2009/2010, an ablation rate of 9.3-m ice equivalent/a was measured at QAS_L; the highest annual recording in Greenland (Fausto, Van As, & Promice Project Team, 2012; Machguth, et al., 2016). The largest recorded daily ablation rate of 28-cm ice/day originates from QAS_L on 11 July 2012, when 2.7-m daily average air temperature reached 12.1 °C (Fausto, van As, Box, Colgan, & Langen, 2016). Causes of extremes in Greenland surface melt involve persistent atmospheric circulation anomalies (Fettweis et al., 2013), atmospheric rivers that deliver intense heat and moisture (Neff et al., 2014), and the changing position and amplitude of the northern planetary Rossby wave (Tedesco et al., 2016).

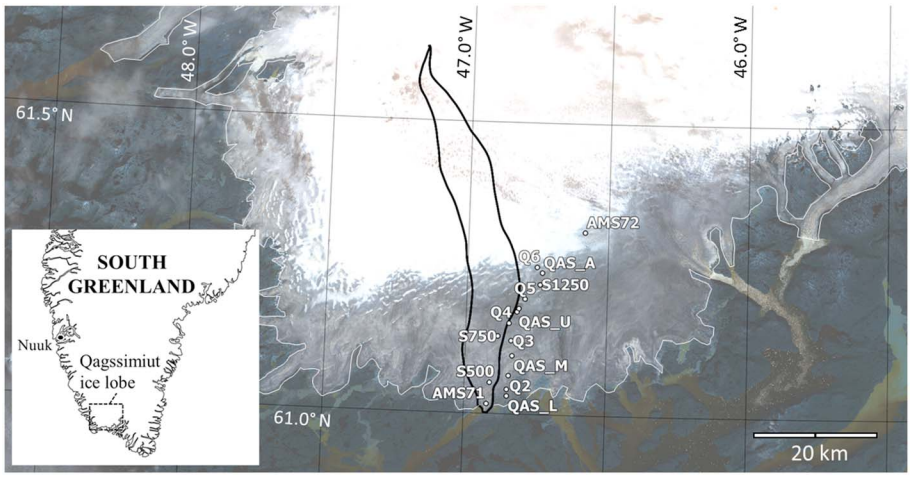

Figure 1. The Q-transect on the Qagssimiut ice lobe in southern Greenland. Observation locations are indicated with white dots. The Sermilik glacier catchment is shown using a black line that extends from 61.00°N to 61.63°N and 46.81°W to 47.20°W. The background image was acquired by the European Space Agency Sentinel-2 satellite, merged band 2/blue, 3/green and 4/red (Drusch et al., 2012) on 28 August 2016 and clearly indicates the bare ice area (dark pixels) below snow line near equilibrium line altitude. The ice sheet outline is indicated by a white line.

A study by Podlech et al. (2004) of the Sermilik glacier on the Qagssimiut ice lobe in south Greenland (Figure 1) found that changes in surface mass balance (SMB) explained 55% of the glacier's thinning between 1985 and 2000. Increased ice velocities accounted for the remaining mass loss. In the 15 survey years, the Sermilik glacier thinned more than 120 m near its calving front and 53 m on average over a line extending 35 km inland. Enderlin et al. (2014) estimated annual dynamic ice flow discharge from the Sermilik catchment from 2000–2012, with values suggesting a 75% increase in dynamic discharge between 2000 and 2009, followed by reduction back to the 2000 level by 2012. They suggested that SMB will remain the dominant factor of Greenland ice sheet mass loss in the foreseeable future.

During the Holocene thermal maximum (9–5 ka BP), when temperatures were 2–4 °C above present, the southwestern ice margin retreated 40–60 km inland from its present-day extent (Larsen et al., 2015; Lecavalier et al., 2014). Deglaciation occurred fast at the Qagssimiut ice lobe (retreat of 30–95 m/a), likely because of oceanic influence enhancing basal melt and calving in a warming climate (Winsor et al., 2015).

Enhanced knowledge of regional scale mass balance is gained through the application of regional climate models (RCMs) forced by global meteorological gridded observational analyses (e.g., Box et al., 2004; Ettema et al., 2009; Fettweis, 2007; Lucas-Picher et al., 2012). The dependence on global models as well as numerical representation, model physics, empirical parameterizations, and grid resolution determines RCM performance, emphasizing the need for RCM validation with in situ measurements (e.g., Charalampidis et al., 2016; Rae et al., 2012). Further, the Qagssimiut ice lobe stands out as a region of persistent RCM disagreement with observations (Noël et al., 2016, 2017, 2018; Langen et al., 2017).

In this study, we document an expanded set of in situ SMB observations (now 17 balance years and 9 regular locations) and examine what the observations show about spatial patterns of SMB, emphasizing net annual snow accumulation and equilibrium line altitude (ELA). A secondary aim of the study is to evaluate HIRHAM5, Regional Atmospheric Climate Model (RACMO2.3p2), and Modèle Atmosphèrique Régional (MAR) v3.7 RCM accumulation and SMB accuracy using the in situ measurements. We delineate the Qagssimiut ice lobe Sermilik glacier to constrain a surface and total mass budget estimate of the catchment by combining calibrated RCM SMB values with dynamic ice discharge data.

2. Data and Methods

2.1. The Q-Transect

Surface ablation and accumulation field observations have been gathered by the Geological Survey of Denmark and Greenland (GEUS) at the Qagssimiut ice lobe, hereafter Q-transect starting in year 2000 (Figure 1). Two automatic weather stations (AWSs) of the Ice Monitoring project—referred to as AMS71 and AMS72—recorded surface energy budget (SEB), meteorological parameters and ice ablation between

Table 1
The 22 Snow Accumulation Observations for 2013/2014, 2014/2015, and 2016/2017 Accumulation Seasons

				Balance year		
Latitude[a](°N)	Longitude[a](°W)	Elevation[a](m)	Site	2013/2014	2014/2015	2016/2017
61.0310	46.8488	288	QAS_L	0.4 ± 0.1	0.3 ± 0.1	0.6 ± 0.2
61.0428	46.8493	420	Q1	0.5 ± 0.2	0.3 ± 0.0	0.6 ± 0.2
61.0661	46.8439	530	Q2	0.4 ± 0.2	0.2 ± 0.1	0.6 ± 0.3
61.0999	46.8329	660	QAS_M			1.0 ± 0.3
61.1257	46.8379	766	Q3		1.0 ± 0.4	0.8 ± 0.2
61.1566	46.8471	867	Q4		1.2 ± 0.4	1.1 ± 0.3
61.1329	46.8850	870	S750	0.9 ± 0.3		
61.1761	46.8184	898	QAS_U	1.1 ± 0.2	1.4 ± 0.3	1.2 ± 0.2
61.1976	46.7928	968	Q5			1.0 ± 0.3
61.2436	46.7330	1,008	QAS_A		1.3 ± 0.4	
61.2592	46.7499	1,134	Q6		0.8 ± 0.2	0.9 ± 0.4

Note. Units are in mWE.
[a]Average value during the measuring period at each site, except for 2017 coordinates, which are from single-frequency Global Positioning System measurements. For QAS_M and Q5 (only 2017 observation), coordinates and elevation originate from August 2016 visit.

2000/2001 and 2006/2007 on the Qagssimiut lobe (Van As et al., 2009). Podlech et al. (2004) compiled Ice Monitoring AWS (Bøggild & Podlech, 2006) and ablation stake data (sites S500, S750, S1000, and S1250). In 2007, the Programme for Monitoring of the Greenland Ice Sheet (PROMICE) was initiated, focusing on measurements in the ablation area around the Greenland ice sheet (Ahlstrøm et al., 2008). The PROMICE AWS QAS_L was set up in 2007 and relocated 1.5 km east in 2009 to avoid a crevassed area. Measurements at QAS_U started in 2008. The QAS_A site near equilibrium line was initiated in 2012 and discontinued in 2015. The QAS_M site was established in 2016. In effort to increase spatial sampling and to better understand local-scale SMB variability, six stake locations (Q1, Q2, Q3, Q4, Q5, and Q6) along a line of ~27 km with an elevation span of ~850 m were initiated September 2013 (Figure 1). Annual end of accumulation season (springtime) snow surveys was started in 2014 to better constrain mass inputs to the surface mass budget.

The southern Greenland ice sheet can have extensive melt episodes in winter, complicating the definition of accumulation and ablation seasons. At the lowest Q-transect location (QAS_L) substantial ablation can occur in winter.

2.2. Snow Accumulation

To represent the mass input in the SMB, cold season (approximately September to approximately April) snow water equivalence (SWE) was estimated from near end of accumulation season snow pits and coring at Q-transect ablation area locations during April and May 2014, 2015, and 2017 surveys (Table 1). Year 2017 cores between 60 and 343 cm in depth were obtained using a Kovacs Mark III corer taking a 7.25-cm-diameter sample consisting of snow and refrozen melt layers. The larger diameter (8.9 cm) Kovacs Mark II corer was found to keep snow cores more intact.

In an effort to represent local spatial variability of snow layer thickness (accumulated over glacier ice in the ablation area since the end of the preceding ablation season), several snow-probing measurements are made at each coring site. The average number (N) of snow probings per site was eight in 2014, four in 2015, and nine in 2017. By representing snow layer thickness with an average of snow depth, SWE can be estimated in a more robust way. SWE [mWE = 10^3 kg/m^2] (as shown in Table 1) equals the product of weighed average site snow density [kg/m^3], average snow height [m] and factor 10^{-3}. Density profiles were obtained between one and four times for each Q-transect site depending on available time during fieldwork.

A site-specific snow density error estimate is based on measurement uncertainty and spatial variability (according to the number of snow cores and snow pits per site) as well as using quality notes made during fieldwork (Text S1 in the supporting information). At PROMICE, AMS and S750 sites, the end of the melt season dates marking the beginning of the accumulation season is estimated from Podlech et al. (2004) and Machguth et al. (2016). Linear regression of the relation between end of melt date and associated ablation at

Table 2
Refined Measurements from Podlech et al. (2004), IceMon, PROMICE, and Other Reports

Latitude[a] (°N)	61.0179	61.0535	61.1812	61.2231	61.3135
Longitude[a] (°W)	46.9134	46.9102	46.8143	46.7414	46.5838
Elevation[a] (m)	272	518	950	1,013	1,150
Balance year	AMS71	S500	S1000	S1250	AMS72
2000/2001	−5.3		−0.4		
2001/2002	−5.9	−3.2		0.3	
2002/2003	−7.2			−0.6	0.6
2003/2004	−5.5				
2004/2005	−5.3				
2005/2006	−5.1				
2006/2007	−6.2				
		PROMICE introduction			
Latitude* (°N)	61.0297		61.1772	61.2442	
Longitude* (°W)	46.8535		46.8177	46.7332	
Elevation* (m)	291		902	1,011	
Balance year	QAS_L		QAS_U	QAS_A	
2007/2008	−6.6		−0.7		
2008/2009	−3.7		0.3		
2009/2010	−8.4		−2.7		
2010/2011	−4.2		−0.7		
2011/2012	−7.7		−1.9		
2012/2013	−5.3		−0.1	−0.1	
2013/2014	−5.5		−1.5	−1.3	
2014/2015	−4.6		0.4	0.6	
2015/2016	−6.8		−1.8		
Average	−5.8	−3.2	−0.9	−0.2	0.6
σ	1.2	–	1.0	0.7	–

Note. Average and standard deviation (σ) refer to an entire column. Units are mWE.
[a] Average value during the measuring period at each site.

the PROMICE AWS sites resulted in the end of melt season dates (and therefore the start of the accumulation season) at the six stake locations (Q1 … Q6). Accumulation season end dates are approximated by the spring visit dates, which spanned from 21 April to 5 May (Text S2 and Table S1). Here accumulation and ablation rates refer to hydrological balance years.

2.3. Ice Ablation and SMB

An updated set of annual ablation observations containing 50 in situ SMB measurements are presented here. The update includes some refinements to data presented in Machguth et al. (2016), namely, accounting for position change in time (latitude, longitude, and elevation) and modifications of start and end date of balance years (Text S3 and Table S2) after Podlech et al. (2004; Table 2). The new data set includes data from six new ablation stakes surveyed after September 2013 installation (Table 3). Positions and time intervals of each balance year are listed in Table S2. SMB was converted to meters water equivalent (mWE) assuming ice density to be 900 kg/m^3.

2.4. Sermilik Glacier Basin Delineation

In Podlech et al. (2004), the catchment was approximated by three parallelograms between AMS71 and S1250 (Figure 1), mainly located in the ablation zone, according to Global Positioning System observations from 2000 and 2001. Glacier basins may be defined by hydrological drainage (e.g., Van As et al., 2014). New high-resolution (250 × 250 m) bed elevation maps reveal complex behavior in which subglacial drainage patterns compete between catchments depending on seasonal changes in basal water pressure (Lindbäck et al., 2015). Here lacking detailed bed mapping, we define the Sermilik glacier catchment solely using 500-m

Table 3
Stake SMB Measurements From GEUS Add Six Additional Data Points on the Q-Transect Since Balance Year 2013/2014

Latitude[a](°N)	61.0427	61.0660	61.1257	61.1566	61.1981	61.2593
Longitude[a](°W)	46.8492	46.8440	46.8379	46.8471	46.7924	46.7505
Elevation[a](m)	417	528	766	867	970	1,135
Balance year	Q1	Q2	Q3	Q4	Q5	Q6
2013/2014	−4.5	−2.7	−2.6	−1.8	−0.8	−0.6
2014/2015	−4.1	−2.5	−0.1	−0.3		−0.3
2015/2016	−5.9	−3.7	−2.5	−2.6	−0.5	−0.7
Average	−4.9	−3.0	−1.7	−1.6	−0.6	−0.5
σ	0.8	0.5	1.2	1.0	0.2	0.2

Note. Units are mWE.
[a]Average value during the measuring period at each site.

gridded surface velocities obtained from the Sentinel-1 satellite (Nagler et al., 2015) from acquisitions between December 2015 and March 2016. The observed velocity field is taken as an approximation of the flow field that delivers both ice and surface runoff to the glacier front. The ice at the glacier front moves with velocities of 0.55 to 0.6 km/a. In the middle of the catchment, velocities of ~0.1 km/a are observed. Streamlines are produced from the velocity field using the MATLAB *streamslice* function (Figure 2). The basin's outline was then identified by tracing the streamlines backward from the outermost glacier front positions, also defined as watersheds at the ice sheet margin. We note that some areas, including the QAS_L location, do deliver meltwater to the Sermilik fjord but lie outside the drawn catchment borders.

The surface elevation of the catchment area is derived from the 27 January 2017 Arctic digital elevation model (ArcticDEM) (Morin et al., 2016). National Aeronautics and Space Administration's Operation IceBridge laser altimeter observations (Studinger et al., 2015) of 14 May 2016 were used to identify the need to adjust the ArcticDEM surface elevation everywhere by −5.4 m. The IceBridge flight line was a few hundred meters east of the catchment area, designed to cover the Q-transect and reaching up to about 1,000 m in elevation. The elevation profiles along a central Sermilik glacier flow line and along the Q-transect are illustrated in Figure 3. The ArcticDEM did not cover Q5 and Q6, which is why the elevation profile deviates from these sites. Overall, Sermilik glacier spans from sea level to 1,775 m in elevation. In line with a first-order Euler approximation of the surface integral, the glacier's surface area measures 559 km^2.

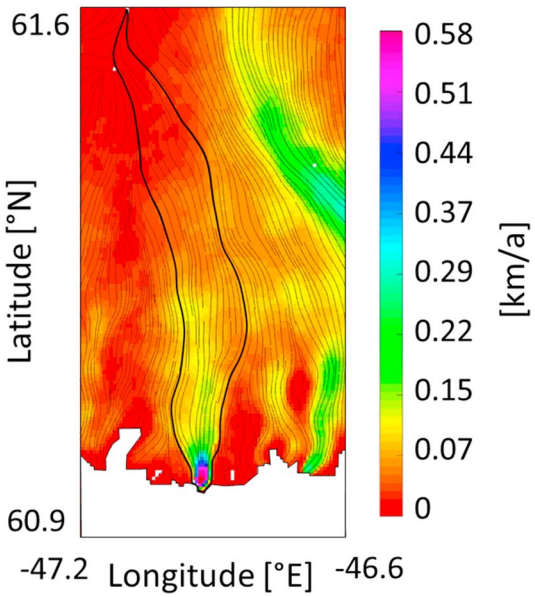

Figure 2. Ice velocity map of the Sermilik glacier catchment and surrounding regions from Sentinel-1 data after Nagler et al. (2015). Thin black lines indicate ice flow lines. The estimated catchment outline is shown using thicker black lines.

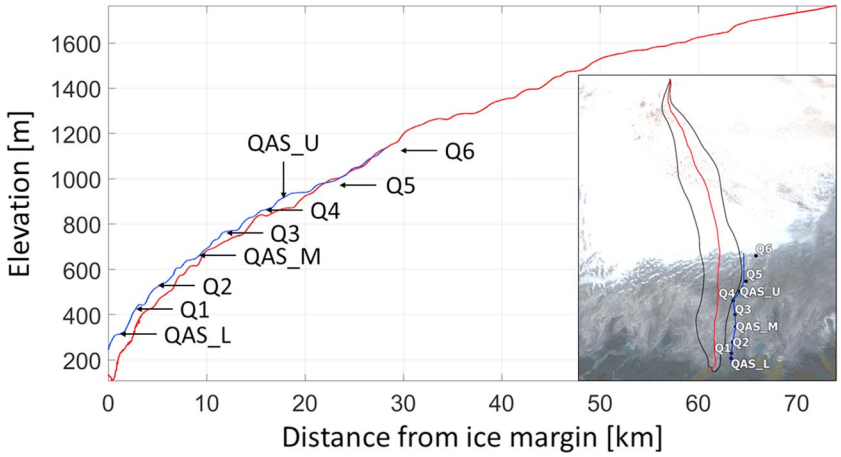

Figure 3. Elevation profile of Sermilik glacier along a central flow line (red lines) and along the Q-transect (blue lines) according to the National Aeronautics and Space Administration Operation IceBridge (−5.4 m) adjusted Arctic digital elevation model. The inset graphic indicates the profiles seen from above. Arrows pointing onto the blue Q-transect line indicate actual site positions, except for Q5 and Q6 that deviate from this line.

2.5. Regional Climate Models

2.5.1. HIRHAM5

The HIRHAM5 hydrostatic RCM (Christensen et al., 2007) is developed by the Danish Meteorological Institute and the Potsdam Research Unit of the Alfred Wegener Institute Foundation for Polar and Marine Research. HIRHAM5 combines the semi-Lagrangian dynamics of the High Resolution Limited Area Model version 7 (HIRLAM7) weather forecast model (Undén et al., 2002) with the physical parameterization schemes of the ECHAM5 climate model (Roeckner et al., 2003), which includes the parameterized convection scheme of Tiedtke (1989) as modified by Nordeng (1994). In the current configuration, HIRHAM5 is run over a Greenland-wide domain at 5.5-km resolution (0.05° × 0.05° on a rotated pole grid; Lucas-Picher et al., 2012) with 31 vertical levels in the atmosphere.

Six-hourly inputs of horizontal wind vectors, temperature, and specific humidity from the ERA-Interim reanalysis data set (Dee et al., 2011) are supplied at the domain boundaries at all atmospheric levels to compute the atmospheric circulation within the domain at 90-s time steps. The resulting surface fluxes of energy (turbulent and downward radiative) and mass (snow, rain, evaporation, and sublimation) are used to drive an off-line snow/ice subsurface scheme, which provides SMB, runoff and refreezing rates (as in Langen et al., 2015, 2017). The subsurface model was extended by Langen et al. (2017) to include 32 model levels, snow densification, varying hydraulic conductivity, irreducible water saturation, and other effects on snow liquid water percolation and retention. Surface albedo is taken as Moderate Resolution Imaging Spectroradiometer-derived daily gridded fields of observed surface albedo after Box et al. (2012). HIRHAM5 output was available from 2000 to 2016, that is, in balance years 2000/2001 – 2015/2016, in the region of the Q-transect. The Sermilik glacier is represented by 13 grid elevations and was linearly interpolated for direct comparison with the Q-transect sites (section 3.4). To compare HIRHAM5 with observed accumulation rates (section 3.4.1), the daily SMB rates were integrated over the winter accumulation season. That corresponds to SMB integrated over time between minimal cumulative SMB in fall (earliest 1 September) and maximal cumulative SMB in spring (latest 31 May). Interpolated HIRHAM5 output was further compared to observed SMB values and in the ablation area, calibrated HIRHAM5 SMB-elevation profiles over each hydrological balance year served together with the delineated basin (section 2.4) in estimating total SMB of the Sermilik glacier catchment (section 3.6). The SMB elevation profiles were extrapolated by a linear ablation area SMB regression for the 2% of the total glacier area below the lowest grid point at 289 m and SMB simulated at the highest grid point (1,601 m) served filling the data gap of 9% of glacier area above.

2.5.2. Modèle Atmosphèrique Régional

The RCM MAR (Gallée & Schayes, 1994; Fettweis, 2007; Fettweis et al., 2017) includes a snow and ice part of its surface scheme based on the CROCUS snow model (Brun et al., 1992). It allows meltwater refreezing and snow metamorphosis, influencing the transformation of snow to ice and the surface albedo using the CROCUS formulations (Brun et al., 1992; Galleé et al., 2001). The MAR physical parameterizations used here

are the ones from Fettweis et al. (2017), which are calibrated to agree with the satellite derived melt extent over 1979–2009. The snowpack initialization is described in Fettweis et al. (2005). Daily MAR version 3.7 simulations using ERA-Interim forcing output at 7.5-km native resolution are resampled to the Vernon et al. (2013) 5-km grid for the 2000 to 2016 period.

MAR version 3.7 is not significantly different, that is, only bug corrections and some adjustments of parameters, as compared to MAR version 3.5.2. (Fettweis et al., 2017). Sermilik glacier was represented by 26 elevations in MAR. MAR snow accumulation and SMB comparison with in situ measurements (section 3.4) were derived similarly to HIRHAM5. The SMB-elevation profiles of MAR were extrapolated linearly for the 0.2% of the total glacier area below the lowest grid point at 76 m and SMB at the highest grid point (1,594 m) filled the gap for the 9% of glacier area above.

2.5.3. Regional Atmospheric Climate Model Version 2

The Regional Atmospheric Climate Model (RACMO2) (Van Meijgaard et al., 2008) incorporates the dynamical core of the HIRLAM (Undén et al., 2002) and the physics package cycle CY33r1 of the European Centre for Medium-range Weather Forecasts Integrated Forecast System (ECMWF-IFS, 2008). Over land ice, the polar version of RACMO2 incorporates a multilayer snow module that simulates melt, liquid water percolation and retention using a tipping bucket approach, refreezing and runoff (Ettema et al., 2010), and accounts for dry snow densification following Ligtenberg et al. (2011). Snow albedo is based on prognostic snow grain size, cloud optical thickness, solar zenith angle, and impurity content (Kuipers Munneke et al., 2011), the latter being prescribed as constant in time and space. The model simulates drifting snow transport and sublimation following Lenaerts et al. (2012). Over Greenland and its surroundings, RACMO2 is forced at the lateral boundaries by ERA-Interim, with upper air relaxation as in Van de Berg and Medley (2016), run at a resolution of ~11 km horizontally and 40 vertical layers. Statistical downscaling of RACMO2.3 version p2 (hereafter RACMO2) is used to increase the resolution over the ice sheet to 1 km, in order to better resolve the steep coastal margins and narrow outlet glaciers (Noël et al., 2016). Sermilik glacier was represented by 239 elevations in downscaled RACMO2. Its lowest grid point is below minimal Sermilik glacier height and SMB at the highest grid point (1,736 m) was taken for the 0.5% of glacier area above. RACMO2 snow accumulation and SMB comparison with in situ measurements (section 3.4) was derived similarly to HIRHAM5.

3. Results and Discussion

3.1. Snow Accumulation

Observed net snow accumulation (Table 1) is equivalent at the three lowest sites (QAS_L, Q1, and Q2) between 285- and 528-m elevation, then approximately doubles for sites with elevation between 660 (QAS_M) and 1,008 m (QAS_A). Minimum snow accumulation near the ice margin is also observed along the K-transect at 67°N on the western ice sheet (van den Broeke et al., 2008). Annual precipitation totals at coastal stations surrounding the Qagssimiut ice lobe, that is, Paamiut ~900 mm; Ivittuut ~1,350 mm; Qaqartoq ~900 mm; Ikerasassuaq ~1,900 mm; Narsarssuaq ~600 mm (Mernild et al., 2015) are roughly 30% higher than the SWE measured on the lowest Q-transect sites (Q1, Q2, and QAS_M; Table 1). The lower on-ice values appear to result from ~1/3 of the precipitation at the lowest Q-transect sites falling as rain. The rain can be lost from the snow profile when percolating below the snow sampling profile and draining away into crevasses and preferential flow paths. New 2016/2017 tipping bucket rain gauge data from the QAS_M station indicate rain events totaling at least 270 mm for the year.

The peak accumulation at 898 m (QAS_U), measuring 1.1 (in 2013/2014), 1.4 (in 2014/2015), and 1.2 mWE (in 2016/2017) appears to be orographic given: (1) the observed accumulation decrease from QAS_U to the higher elevation of QAS_A (2014/2015), Q5 (2016/2017), and Q6 sites; (2) an inland decrease in accumulation in maps based on interpolation of ice cores, RCM output, or combinations of the two (e.g., Box et al., 2004; Burgess et al., 2010; Lucas-Picher et al., 2012; Ohmura & Reeh, 1991; Ohmura et al., 1999); (3) estimates of the snow accumulation peak on the Q-transect are ~1.7 mWE (Box et al., 2004) and ~1.4 mWE (Burgess et al., 2010) between roughly 800- and 1,300-m elevation. Further, the spatial pattern of snow accumulation on the Q-transect is consistent among the 3 years of observation.

Snow surface height is measured by PROMICE AWS every 10 min by sonic ranging sensors facing downward from two placements: a stake frame 5–15 m from the AWS and the AWS horizontal arm. 22 coincident snow height and accumulation rate measurements (Table S1) starting on 5 May 2014, that is, in balance year 2013/2014, here compared in regression suggest snow height is a satisfactory predictor (R^2 = 0.91) of SWE

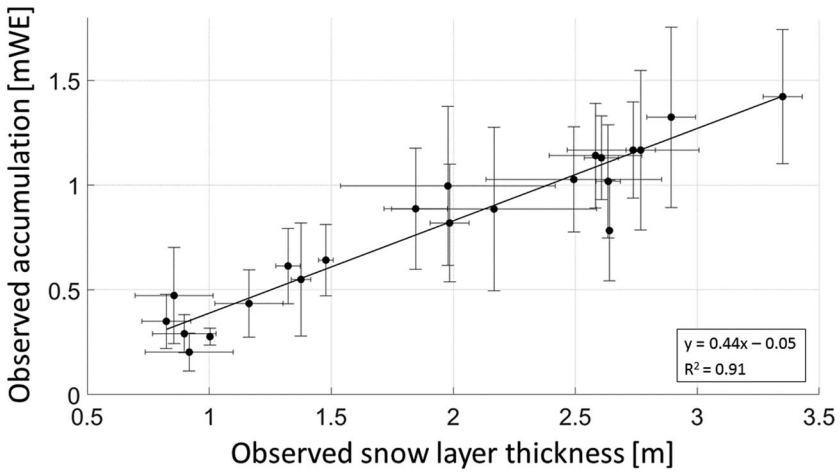

Figure 4. Observed accumulation and snow height from the 22 observations during springtime visit including an orthogonal linear regression fit. Horizontal uncertainty "whiskers" represent one standard deviation (σ) of the snow height measurements. Vertical whiskers represent the error estimate of accumulation described in methods.

(Figure 4) consistent with Sturm et al. (2010). The effectively zero (−0.05 mWE) *y* intercept implies a constant bulk (depth averaged) density of 441 kg/m^3 for all sites on the Q-transect. This bulk density value is within 2% of the value (430 kg/m^3) found from May 2003 field measurements (Podlech et al., 2004), indicating no temporal change in bulk snow density on the Q-transect during 14 years. It thus seems that we may estimate SWE for places and dates that only have snow thickness available, that is, from other AWS surface height records obtained by PROMICE Q-transect stations.

The empirical fit (Figure 4) is used to estimate accumulation rate given snow surface height from sonic ranger snow thickness data spanning 2007/2008 (QAS_L) or 2008/2009 (QAS_U) until 2012/2013. From this approximation, we obtain 11 additional synthetic end of accumulation season SWE values (section 3.4.1). Before we apply our accumulation estimates to examine RCM accumulation accuracy, we first evaluate RCM SMB estimates.

3.2. Ablation Area SMB

From the field observations, we determine average SMB at the AWS and ablation stake sites (Tables 2 and 3). At QAS_L, record setting net annual ablation of 8.4 mWE was measured in August 2010, exceeding the 2000/2001 – 2015/2016 average by 2.1σ. At the upper (QAS_U) station, 2009/2010 ablation of 2.7 mWE was

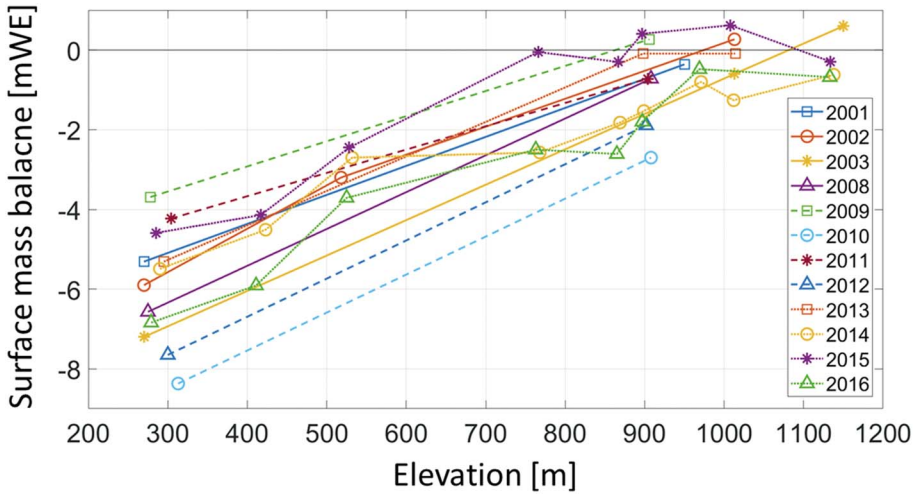

Figure 5. Annual surface mass balance measurements recorded at Q-transect sites in years with two or more observations. The legend indicates the end year of each balance year, for example, 2001 stands for balance year 2000/2001.

Table 4
Results From a Yearly Linear Fit of the Observed SMB (Tables 2 and 3) and the Model-Based Balance Gradient and SMB at 0 m a.s.l.

	Balance gradient (mWE/km)				SMB at 0 m a.s.l. (mWE)				ELA (m)		
Balance year	OBS[a]	HH5/OBS	MAR/OBS	RACMO2/OBS	OBS[a]	HH5/OBS	MAR/OBS	RACMO2/OBS	OBS	N. observations	R^2
2000/2001	7.3	0.56	0.74	0.63	−7.3	0.65	0.89	0.59	999	2	—
2001/2002	8.1± 0.6	0.62	0.69	0.63	−7.8 ± 0.4	0.54	0.77	0.38	963	3	0.99
2002/2003	8.9 ± 0.0	0.47	0.67	0.61	−9.6 ± 0.0	0.57	0.80	0.53	1,082	3	1.00
2007/2008	9.2	0.42	0.52	0.59	−9.1	0.53	0.68	0.57	986	2	—
2008/2009	6.3	0.52	0.75	0.68	−5.4	0.50	0.99	0.49	863	2	—
2009/2010	9.5	0.43	0.64	0.57	−11.4	0.56	0.77	0.55	1,191	2	—
2010/2011	5.9	0.58	0.75	0.75	0.60	0.63	0.92	0.54	1,027	2	—
2011/2012	9.6	0.28	0.60	0.49	−10.5	0.37	0.75	0.44	1,100	2	—
2012/2013	7.7 ± 0.8	0.36	0.57	0.52	−7.5 ± 0.6	0.40	0.71	0.43	973	3	0.98
2013/2014	5.6 ± 0.3	0.46	0.82	0.79	−6.6 ± 0.2	0.55	0.94	0.65	1,193	9	0.93
2014/2015	6.4 ± 0.6	0.39	0.58	0.66	−6.1 ± 0.4	0.29	0.70	0.36	949	8	0.84
2015/2016	7.5 ± 0.4	0.40	0.67	0.49	−8.6 ± 0.3	0.51	0.83	0.53	1,138	8	0.93
Average	7.7	0.46	0.67	0.62	−8.0	0.51	0.81	0.50	1,039	—	—
σ	1.4	0.09	0.08	0.09	1.8	0.10	0.10	0.08	98	—	—

Note. Balance gradients for each model include all points below highest SMB < 0 mWE and one grid point above. a.s.l. = above sea level.
[a] The observed annual balance gradient and SMB at 0-m elevation include uncertainty resulting from one standard deviation of regression parameters (determined by the MATLAB function polyparci for a 68.2% confidence interval). The bottom rows show mean and standard deviation (σ) for variables. SMB = surface mass balance; ELA = equilibrium line altitude; OBS = observations.

1.8σ above the 2000/2001 and 2007/2008–2015/2016 average. The observations indicate that annual ablation at QAS_L varies by more than a factor of 2 between a year with low ablation, for example, 2008/2009, and the record warm years with high ablation, 2009/2010 and 2011/2012 (e.g., Fausto, van As, Box, Colgan, Langen, & Mottram, 2016). At QAS_U, ablation in 2013/2014 (−1.5 mWE) and 2015/2016 (−1.8 mWE) was comparable to that in 2011/2012 (−1.9 mWE), due to low winter accumulation (Figure 7 for 2013/2014), reminding us of the importance of snow accumulation in reducing ice ablation rates.

3.3. SMB Versus Elevation

As in earlier work (e.g., Braithwaite, 1984; Van de Wal et al., 2012), we find the elevation dependence of SMB to be well approximated ($R^2 \geq 0.84$) by linear regression (Figure 5 and Table 4). Application of a linear fit of elevation and SMB < 0 mWE only to other PROMICE regions (Fausto, van As, Ahlstrøm, Andersen, et al., 2012) and KAN represented by K-transect data after Van de Wal et al. (2012, Table 5) indicates that the average

Table 5
Greenland Ice Sheet SMB Gradients in the Ablation Area Including One Standard Deviation of the Years Used From PROMICE Regions

PROMICE region	Average latitude (°N)	Average longitude (°W)	Average elevation (m)	SMB gradient below ELA (mWE/km)	σ (mWE/km)	Average no. of sites per year	No. of years used
QAS[a]	61.15	46.80	733	7.4	1.6	4.1	9
NUK	64.65	49.56	860	5.5	0.6	2.3	10
KAN[b]	67.05	48.60	1263	3.8	0.6	6.4	18
THU	76.41	68.21	670	6.3	1.0	2.0	6
KPC	79.87	24.63	620	4.0	0.9	2.0	7
SCO	72.31	27.03	725	2.0	0.4	2.0	9
TAS	65.71	38.89	577	2.6	1.2	2.2	10

Note. Gradient results from linear regression of PROMICE AWS and stake reading SMB < 0 mWE only.
[a] We note that average SMB gradient at QAS slightly differ from the result in Table 4 for comparability to other PROMICE regions as here, we include (1) PROMICE AWS and stake observations but no other literature such as Podlech et al. (2004) and (2) positive SMB measurements only. [b]KAN data are after Van de Wal et al. (2012). SMB = surface mass balance; PROMICE = Programme for Monitoring of the Greenland Ice Sheet; ELA = equilibrium line altitude; mWE = meters water equivalent; AWS = automatic weather station.

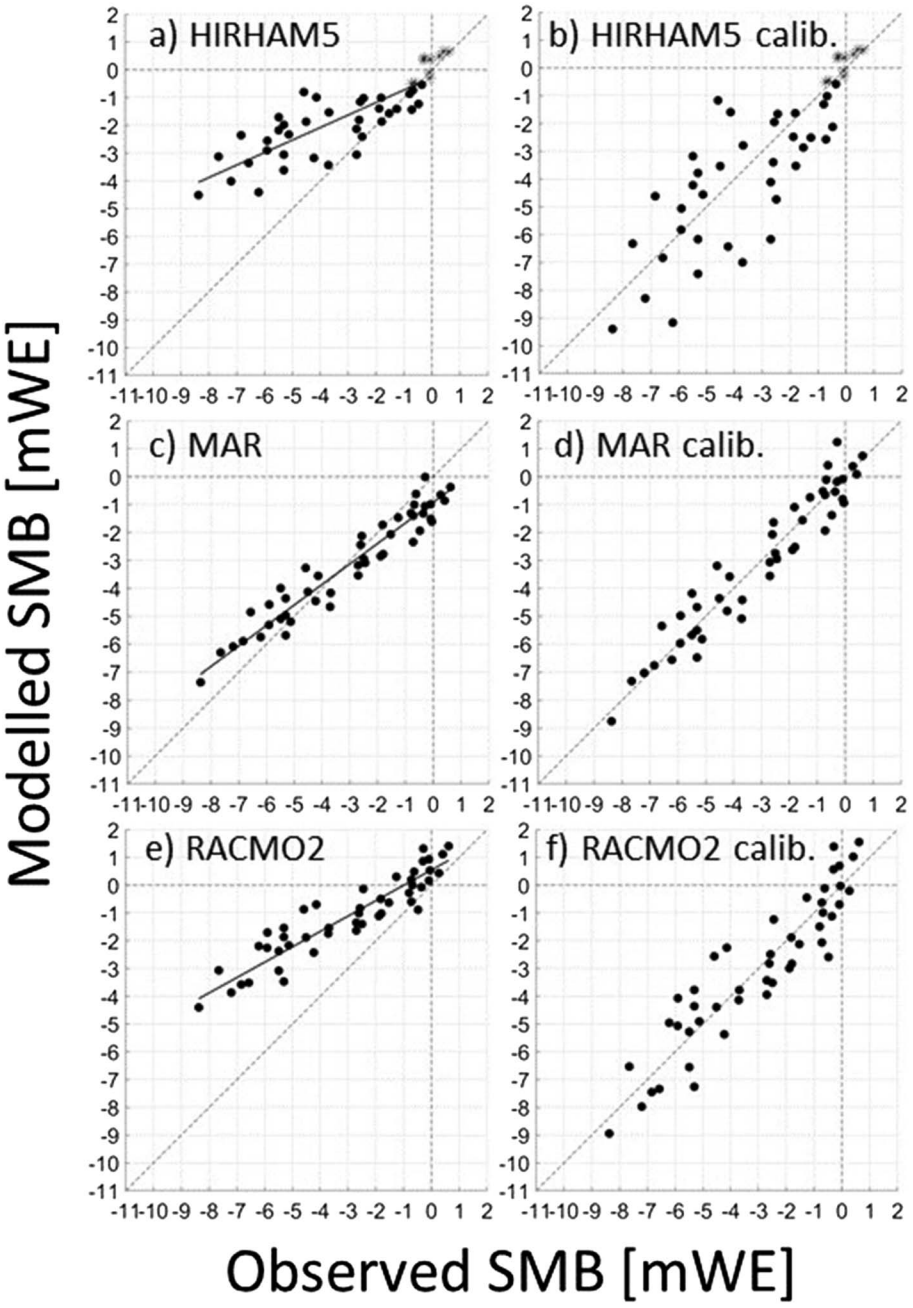

Figure 6. Modeled and observed SMB at the Q-transect sites for a) HIRHAM5, c) MAR and e) RACMO2 (all 2000/2001–2015/2016). In a) linear fit through (−0.5, −0.5) and in c) and e) orthogonal trend lines, used for calibration, are shown in black/solid and the diagonal 1:1 line is dashed. b), d) and f) show the calibrated model data (dots), while HIRHAM5 data (b) was not calibrated for SMB above −0.5 mWE (asterisks). SMB = surface mass balance; MAR = Modèle Atmosphèrique Régional; mWE = meters water equivalent.

SMB gradient for the Q-transect (QAS) is higher than elsewhere in the PROMICE (and K-transect) coverage. The higher Q-transect balance profile seems a consequence of high mass turn over that steepens the ice sheet elevation profile.

In years with few (only two or three) SMB observations, the elevation gradient in SMB can be more sensitive to measurement errors, site-specific factors (e.g., if a measurement location is in the bottom of an undulation or near an undulation ridge), and observations being more distant from ELA (especially at extremely low elevations where the influence of marine-based temperature inversions is evident; Ohmura, 1987;

Mernild & Liston, 2010). Therefore, ELA extrapolation may not be sufficient to estimate ELA when including only one or two additional values to that from the lower ablation area. ELA estimated by extrapolation of the SMB profile to SMB = 0 mWE varies between 863 m in 2008/2009 and 1,193 m in 2013/2014, with a 12-year average of $1,039 \pm 98$ m (Table 4). For years with eight or nine observations, the uncertainty of ELA was computed from the standard deviation (σ) of the regression parameters. The Q-transect ELA range is 1,093–1,305 (approximately ±9%) in 2013/2014, 808–1,117 (approximately ±16%) in 2014/2015, and 1,037–1,252 m (approximately ±9%) in 2015/2016.

By extrapolation, we compute an average hypothetical SMB at sea level of -8.0 ± 1.8 mWE over the 12 years of data. Stronger SMB balance gradients coincide with a low SMB at QAS_L (e.g., 2002/2003, 2007/2008, 2009/2010, and 2011/2012). However, the linear assumption appears biased to estimate low ELAs in the case when only two or three observations are available. A low ELA bias may be caused by QAS_L and AMS71 having large ablation rates (Figure 5) owing to extremely low surface ice albedo of ~0.2 (Fausto, van As, Box, Colgan, Langen, & Mottram, 2016). It is thus uncertain whether the factor of 1.7 difference in the calculated balance gradients (5.6 mWE/km in 2013/2014 to 9.6 mWE/km in 2011/2012) is robust. The less extreme balance gradients starting in 2013/2014, when the Q-transect has several more observation points, are more certain due to the larger sample count and more samples near ELA. Van de Wal et al. (2012) find the most satisfactory approximations of ELA by using only negative SMB values and only stations near ELA, that is, K-transect stations S8 and S9, instead of all K-transect values.

3.4. RCM SMB Validation

A significant RCM underestimation of the SMB elevation gradient with elevation is evident (Table 4). Accompanying this bias is an underestimation of SMB near sea level by roughly 2 times by HIRHAM5 and RACMO2 but only 1.2 times by MAR. Figure 6 illustrates the simulated HIRHAM5, MAR, and RACMO2 SMB biases. Where the HIRHAM5 annual SMB is below −0.5 mWE, the bias is approximated ($R^2 = 0.55$) by orthogonal linear regression forced through point (−0.5, −0.5) in Figure 6 with regression coefficients $r_1 = 0.45$ (slope) and $r_2 = -0.27$ (intercept). RACMO2 and MAR bias seemed consistent over the whole SMB observation span, which is why the regression was not restricted to certain values as for HIRHAM5. Orthogonal linear regression coefficients for RACMO2 ($r_1 = 0.55$, $r_2 = 0.55$) and MAR ($r_1 = 0.73$, $r_2 = -0.92$) were higher; $R^2 = 0.85$ and $R^2 = 0.92$, respectively. These regressions are used to calibrate model SMBs used in section 3.6. The factor of 2.2 (=1/0.45) in the HIRHAM5 bias is equivalent with that found by Langen et al. (2017) at QAS_L. RACMO2 shows a similar behavior as HIRHAM5; that is, underestimation of melt in the whole ablation area, however, by a smaller factor of 1.8. MAR SMB has a conditional bias, that is, melt underestimation below SMB = −3.5 mWE and melt overestimation above.

There are several likely factors contributing to the RCM underestimation of ablation for SMB more negative than roughly −0.5 mWE (if not for all of the ablation area). These are discussed in the following, starting with what seems to be the dominant factor: precipitation bias.

3.4.1. RCM Accumulation Validation

We compare HIRHAM5, MAR, and RACMO2 net snow accumulation rates with the Q-transect snow accumulation field observations as the sum of daily RCM SMB between minimum cumulative daily SMB in the fall (earliest 1 September) and maximum cumulative SMB in spring (latest 31 May) from 2013/2014 and 2014/2015 (Figure 7). For comparisons shown in Figure 8, we integrate RCM SMB over the same time period as accumulation field data spans (Table S1).

In 2013/2014 and 2014/2015, when both observational and RCM data are available, HIRHAM5 and RACMO2 show a more than 2 times ablation area wet bias, that is, too much modeled snowfall (Figure 7 and Table 6). RCM data were linearly interpolated to the observation sites. In 2013/2014, the ratio of RCM accumulation, hereafter "RCM"/OBS, is 2.75 for HIRHAM5 and RACMO2/OBS = 2.79 on average at three lowest observation sites (at ~288, ~420, and ~530 m). In 2014/2015, the ratios are 6.90 and 6.30, respectively. For elevations above the orographic precipitation peak at ~800 m, the bias ratios are smaller. Averaged over all observation sites, HIRHAM5 and RACMO2 overestimated accumulation by more than 2 times in 2013/2014 and 3 times in 2014/2015 (Table 6). The HIRHAM5 and RACMO2 average peak values of 2.0-mWE (standard deviation, $\sigma = 0.7$ and $\sigma = 0.6$ mWE, respectively; Figure 7c), exceed the observed accumulation maximum of 1.4 ± 0.3 mWE at QAS_U by a factor of 1.4. Between the accumulation seasons 2000/2001 and 2015/2016, HIRHAM5 and RACMO2 simulate an average peak in accumulation ~140 and ~90 m lower in elevation than the 898-m Q-transect observation peak. At elevations above 1,400 m, HIRHAM5 output suggests a lower

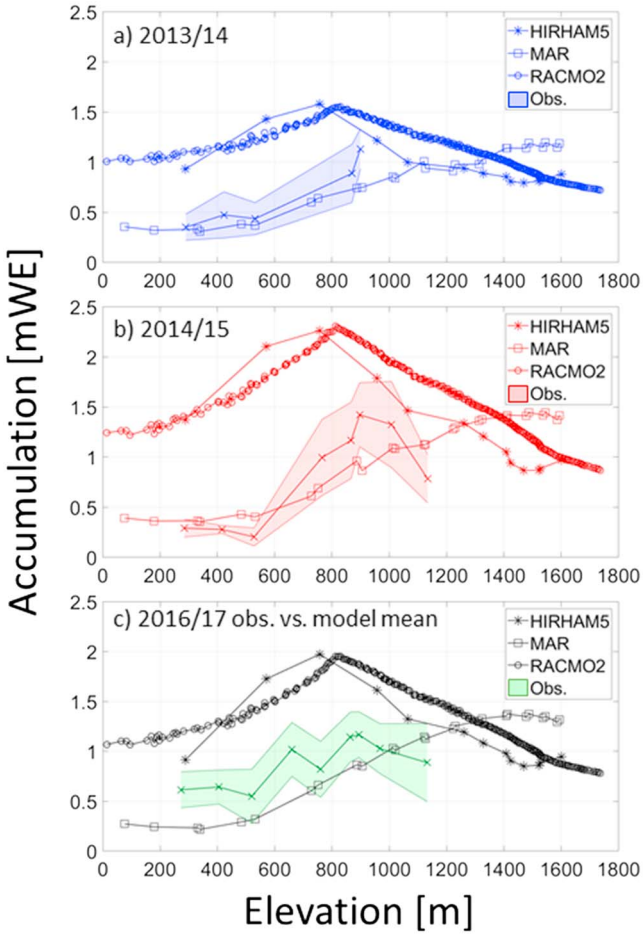

Figure 7. Elevation profiles of observed and modeled net snow accumulation (a) for 2013/2014, (b) 2014/2015, and (c) 2016/2017. A shaded area indicates uncertainty ranges (section 2.2). Black lines in (c) illustrate the comparison of the RCM average for 2000/2001–2015/2016 with the 2016/2017 observations.

accumulation of around 0.8–0.9 mWE (σ = 0.2 mWE), while RACMO2 is decreasing to similar values at slightly higher elevations. Both are comparable to field data from South Dome "a" (0.7 ± 0.1 mWE in 1978–1996) and "b" firn cores (0.7 ± 0.2 mWE in 1986–1996; Box et al., 2013; McConnell et al., 2000). Factors responsible for the peak in accumulation near 800- to 900-m elevation are discussed above (section 3.1).

MAR accumulation is closer in magnitude to the observations than HIRHAM5 or RACMO2. Bias ratios indicate a dry bias in 2013/2014 (MAR/OBS = 0.80 ± 0.09) and a wet bias (MAR/OBS = 1.14 ± 0.44) in 2014/2015 (Table 6). Less realistic than HIRHAM5 and RACMO2, MAR data exhibit no sharp orographic precipitation peak. The maximum average accumulation between 2000/2001 and 2015/2016 of 1.4 ± 0.3 mWE is equal to that observed at QAS_U but located ~500 m higher in elevation at 1,487 m (Figure 7c), rather than around 800–900 m where observations suggest the orographic peak lies. MAR exhibits a ~100-mm wet bias above ELA in comparison with south Greenland ice core-derived values (Fettweis et al., 2017).

Linear regression between RCM and observed accumulation shows a strong deviation from the 1:1 line for HIRHAM5 (Figure 8a) and RACMO2 (Figure 8c). Figure 8, however, suggests larger HIRHAM5 biases for higher accumulation rates (slope = 1.33), while RACMO2 accumulation output is off by a constant factor of +0.80 mWE (slope = 1.06). The MAR trend line (Figure 8b) shows the highest correlation (R^2 = 0.78) among the three RCMs. Especially low accumulation rates are simulated close to the observed values when being compared over the same time period. Regression coefficients (slope = 0.75, intercept = 0.04) show the underestimation of accumulation rates above ~0.5 mWE/a but no constant offset by MAR.

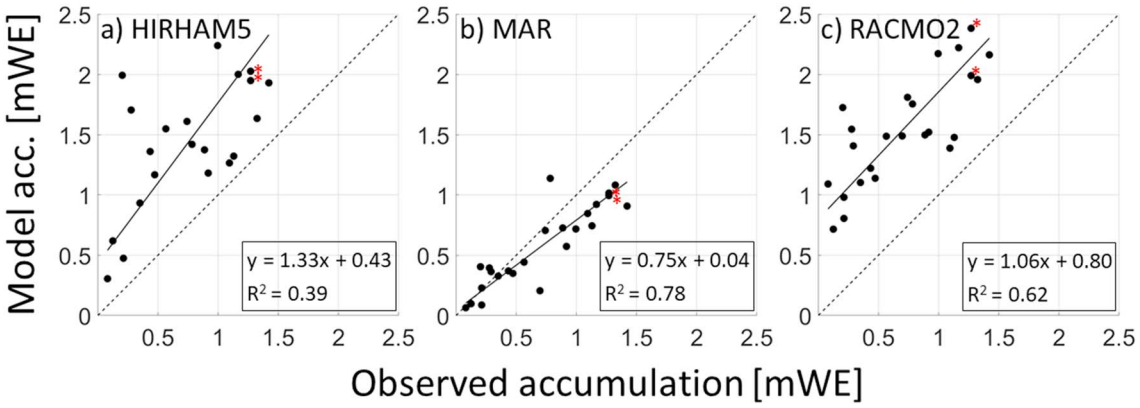

Figure 8. Accumulation derived from ablation area observations and (a) HIRHAM5, (b) MAR, and (c) RACMO2. An orthogonal linear fit line is shown in solid black line for each model, and the 1:1 line is dashed. Red asterisks mark two observed accumulation (2009 and 2012) that was possibly higher than stated to an unknown extent, due to station burial.

Earlier studies have found that precipitation is better represented by increasing HIRHAM5 horizontal grid resolution, for example, from 25 to ~5.5 km (Lucas-Picher et al., 2012). See also Ettema et al. (2009). Langen et al. (2015) already suggested that 5.5-km HIRHAM5 topographic enhancement of precipitation is too effective. Results from Iceland presented by Schmidt et al. (2017) using ~5.5-km HIRHAM5 simulations also show a wet bias on windward slopes.

The three RCMs evaluated in this study invoke the hydrostatic assumption; that is, the upward pressure gradient force is balanced by gravity. Yet unlike computationally expensive nonhydrostatic models, hydrostatic models do not directly simulate vertical atmospheric motion. In addition to the relative computational affordability, the primary justification for the use of hydrostatic models in the polar regions is that little convective vertical motion takes place. However, the hydrostatic assumption is increasingly violated as terrain slope increases, which occurs more frequently as grid resolution is increased and especially near the ice sheet margin where mountainous terrain is common. Van Wessem et al. (2015) conclude that at ~5.5 km, the limit of the hydrostatic assumption likely is reached, and a nonhydrostatic model should be used in effort improve the simulation of precipitation across areas with steep terrain.

A common limitation in current-generation RCMs regarding precipitation is that is that precipitation falls out instantly and thus cannot be advected. In the most recent MAR version (3.7) evaluated here, however, the velocity of precipitation is adjusted to not be infinite, allowing some advection of precipitation and therefore depositing more precipitation inland during onshore flow, explaining the damped spatial precipitation pattern (Figure 7). For RACMO2, next-generation modifications to the cloud scheme (Noël et al., 2018) lead to clouds being sustained at higher elevations, enhancing precipitation further inland, while it decreases precipitation in lower-lying regions.

3.4.2. Turbulent Energy Fluxes

One likely cause of low-biased RCM ablation rates is the simulation of too little nonradiative surface heating during cases of warm air advection (e.g., during strong 9 m/s on-shore high 5-g/kg humidity, 5+ ° C daily average air temperature and advection cases reported by Fausto, van As, Box, Colgan, and Langen (2016) and Fausto, van As, Box, Colgan, Langen, and Mottram (2016). Events like these, here referred to as "heatwaves," are associated with underestimated downward transfer of sensible and latent heat in the one-level so-called "bulk" method turbulent flux calculations.

Warm air advection over melting ice produces a near-surface stably stratified atmosphere. Commonly used Monin-Obukhov stability corrections dampen the calculated turbulent energy fluxes (e.g., Andreas, 1987, 2002). Yet even excluding a stability correction still produces too little melt during the heatwaves (Fausto, van As, Box, Colgan, Langen, & Mottram, 2016). Fausto, van As, Box, Colgan, and Langen (2016) and Fausto, van As, Box, Colgan, Langen, and Mottram (2016) also examined the importance of aerodynamic roughness length for momentum (z_0) over ice using a point SEB model after Van As et al. (2012) and found that an unrealistically large z_0 increase (from 5 to 50 mm) during heatwaves was needed to match independently observed ice ablation.

Table 6
Ratios of Model and Observed Accumulation (RCM/OBS) for Balance Years 2013/2014 and 2014/2015

Elevation (2013/2014)	HH5/OBS	MAR/ OBS	RACMO2/ OBS	Elevation (2014/2015)	HH5/OBS	MAR/OBS	RACMO2/ OBS	Elevation (2016/2017)	MHH5/ OBS	MMAR/ OBS	MRACMO2/ OBS
290	2.66	0.94	3.15	285	4.71	1.25	4.84	273	1.49	0.39	1.94
423	2.47	0.74	2.41	417	6.15	1.43	5.58	405	1.95	0.39	2.00
532	3.13	0.85	2.81	528	9.82	1.99	8.50	520	2.87	0.57	2.59
—	—	—	—	—	—	—	—	660	1.81	0.50	1.57
—	—	—	—	766	2.25	0.72	2.18	760	2.40	0.82	2.20
870	1.55	0.82	1.69	867	1.71	0.79	1.90	863	1.56	0.73	1.67
899	1.17	0.66	1.31	897	1.36	0.64	1.52	893	1.48	0.74	1.61
—	—	—	—	1,008	1.23	0.82	1.48	967	1.55	0.93	1.72
—	—	—	—	1,134	1.81	1.45	2.24	1,132	1.44	1.28	1.72
Average	2.20	0.80	2.27	Average	3.63	1.14	3.53	Average	1.84	0.70	1.89
σ	0.73	0.09	0.69	σ	2.86	0.44	2.37	σ	0.47	0.27	0.31

Note. In 2016/2017, accumulation measurements are related to model average between 2000/2001 and 2015/2016, therefore ratios are named MRCM/OBS. RCM = regional climate model.

Additional insight comes from comparing values for turbulent fluxes derived using bulk method or two-level observations of wind speed, temperature, and humidity with independent eddy covariance measurements. Box and Steffen (2001) made this comparison for the turbulent latent heat flux, finding that the bulk method could not attain sufficient downward energy flux during strong surface temperature inversion cases. The one atmospheric measurement level at PROMICE AWSs requires the bulk method to be used. If the stations had two atmospheric levels, we suspect that more downward energy could be observed from the alternative two-level "aerodynamic method." However, the aerodynamic method can introduce more measurement uncertainty compared to the one-level bulk method, making it difficult to assess its value (Niwano et al., 2015). Today, it seems that an absolute assessment of RCM turbulent energy fluxes can only be made by performing fast (5+ Hz) sampling ultrasonic anemometer and hygrometer measurements on the ice sheet.

In SEB modeling, z_0 may be tuned to minimize the difference between modeled and observed ablation (Brock et al., 2006). Yet assuming z_0 to be constant in space and time is an oversimplification (Smeets & Van den Broeke, 2008a, 2008b). For RCMs, the z_0 values are in general similar to those in SEB modeling using PROMICE weather station data. RACMO2 uses a z_0 value of 1 mm over snow and 5 mm over bare ice, while HIRHAM5 uses z_0 = 1 mm for both snow and bare ice. MAR treats z_0 as a variable that is in part a function of surface snow and ice density with values ranging from 1 to 8 mm for snow and from 10 to 15 mm for bare ice. While RCMs have multiple layers aloft, they calculate turbulent fluxes at the surface using the bulk method similar to our point SEB modeling. Therefore, RCMs probably also underestimate downward turbulent heat transfer during heatwaves (Fausto, van As, Box, Colgan, Langen, & Mottram, 2016) and possibly during other calmer, colder and drier weather conditions.

RCM ablation area snow melt is likely overestimated by overestimating z_0 = 1 mm. Overestimated turbulent heating of snow thus partly compensates for the ablation area snow accumulation "wet bias" in HIRHAM5 and RACMO2. Brock et al. (2006) recommend z_0 values over snow of 0.1 mm, which, if used, would reduce RCM snow melt, resulting in an even less negative SMB, compounding the effect of too much snow accumulation in HIRHAM5 and RACMO2. However, MAR also uses a large roughness length over snow and does not show a similar bias.

The issue of turbulent heat flux calculation during heatwaves needs further study by using ultrasonic anemometers to directly measure turbulent exchange and surface roughness. Only then may we more fully diagnose SEB biases in turbulent heat transfer calculations in point models and RCMs.

3.4.3. Albedo

The representation of surface albedo in RCMs is an important issue for accurately gauging melt energy given that absorbed solar energy is a dominant melt energy source under clear sky conditions. A suggested cause for the HIRHAM5 ablation underestimation has been that average albedo was too high (bias of +0.16 at QAS_L) (Fausto, van As, Box, Colgan, Langen, & Mottram, 2016; Langen et al., 2017). However, using the closest 500-m

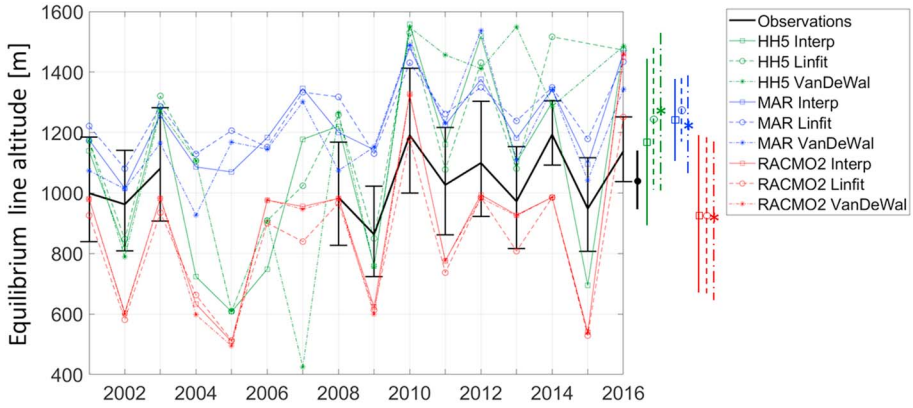

Figure 9. Comparison of equilibrium line altitude estimated from observations and from three regional climate models (RCMs). Three methods are applied to the RCM data to estimate RCM ELA uncertainty. Black whiskers indicate uncertainty of observed ELA. Symbols with whiskers to the right indicate average and one standard variation of the ELA estimates over a 12 years (2000/2001–2002/2003 and 2007/2008–2015/2016) period. ELA = equilibrium line altitude.

National Aeronautics and Space Administration Moderate Resolution Imaging Spectroradiometer MOD10A1 albedo pixel to the QAS_L AWS instead of 5.5-km averaged MOD10A1 albedo pixels used by HIRHAM5, Box et al. (2017) find insignificant albedo bias (within 0.01) in both MOD10A1 collections 5 and 6. HIRHAM5 overestimated albedo at QAS_L thus likely originated from land contamination of the 5.5-km HIRHAM5 grid cell rather than from a systematic bright (too high albedo) bias over the Qagssimiut ice lobe. While a comparison of RACMO2 and MAR versus observed albedo values may further clarify error sources, the comparison with RACMO2.3p2 at 1 km is obscured by the fact that the downscaling procedure applies an elevation and an ice albedo correction to the bare ice albedo prescribed in the original RACMO2 at 11-km resolution; see Noël et al. (2016, 2018). Biases remaining in MAR also suggest that more accurate representation of the bare ice albedo (Fettweis et al., 2017) to include background impurities remains an area of improvement. The MAR bare ice albedo is too high, but this albedo bias is compensated by an overestimation of solar radiation as discussed by Fettweis et al. (2017).

3.4.4. Grid Resolution

Despite "high resolution" by standards of the past decade, the ~5.5-km HIRHAM5 grid size can suffer from being too coarse to resolve narrow ablation areas that occur where accumulation and ablation rates are extremely high and on mountain glaciers and ice caps peripheral to the ice sheet. Yet model resolution seems not the leading cause of the HIRHAM5 underestimation of ablation rates because of bias in the SMB range from −3 to −0.5 mWE (Figure 6) are not mixed with land. Noël et al. (2016) statistically downscaled the polar RCM RACMO2 at 11- to 1-km resolution. The downscaling is shown to improve SMB realism especially in areas of complex terrain. The 1-km downscaling itself, however, only marginally improved the modeled ablation at QAS_L and was followed by melt adjustment reducing the model bias. With MAR, there also remains an underestimation of lower ablation area ice melting.

Finer horizontal resolution than 5.5 km seems necessary to resolve topographic undulations that produce significant (7% to 13%) accumulation variability (Miège et al., 2013). Accounting for wind redistribution of snow and blowing snow sublimation, not parameterized by RCMs seem valuable to increase the accuracy of modeled net snow accumulation.

3.5. Equilibrium Line Altitude

Here we compare Q-transect observed and RCM simulated ELA (Figure 9). For the HIRHAM5, MAR, and RACMO2 RCM, we identified the end of each annual melt season at each grid elevation as the day of minimum cumulative daily SMB. As this method was problematic in the high ablation area where only little ice melt occurs, we restricted end of melt season to be only after 1 July.

The annual elevation profiles of SMB from seasons 2000/2001 to 2015/2016 were used in three approaches to define annual RCM modeled ELA: (a) interpolating between the highest cases with neighboring negative and positive SMB (hereafter, "Interp"), (b) using all values where SMB < 0 mWE for a linear regression extrapolated to SMB = 0 mWE ("Linfit"), and (c) using only the top two SMB model values where SMB < 0 mWE for the regression as in Van de Wal et al. (2012; "VanDeWal"). We use statistics of the differences in the three

Table 7
Catchment-Wide SMB (Σ_{SMB}) Including RCM Dependent Error as Described in the Text

	HH5		MAR		RACMO2		Ensemble	
Balance year	Σ_{SMB}	±	Σ_{SMB}	±	Σ_{SMB}	±	Σ_{SMB}	Spread
2000/2001	−0.5	0.2	−0.3	0.1	−0.3	0.1	−0.4	0.3
2001/2002	0.1	0.1	0.2	0.0	0.5	0.2	0.3	0.4
2002/2003	−1.1	0.5	−0.6	0.1	−0.5	0.1	−0.7	0.6
2003/2004	0.2	0.1	0.1	0.0	0.4	0.1	0.2	0.3
2004/2005	0.5	0.2	−0.0	0.0	0.8	0.3	0.4	0.8
2005/2006	+0.0	0.0	−0.2	0.1	−0.2	0.0	−0.1	0.2
2006/2007	−0.4	0.2	−0.5	0.1	−0.0	0.0	−0.3	0.4
2007/2008	−0.8	0.4	−0.4	0.1	−0.6	0.2	−0.6	0.3
2008/2009	0.2	0.1	0.1	0.0	0.4	0.1	0.2	0.3
2009/2010	−1.9	0.9	−1.0	0.2	−1.3	0.4	−1.4	1.0
2010/2011	−0.4	0.2	−0.2	0.0	0.1	0.0	−0.1	0.5
2011/2012	−0.9	0.4	−0.8	0.2	−0.6	0.2	−0.7	0.3
Average	−0.4	0.3	−0.3	0.1	−0.1	0.1	−0.3	0.5
			Additional years					
2012/2013	−0.1	0.1	−0.1	0.0	0.1	0.0	+0.0	0.3
2013/2014	−0.9	0.4	−0.4	0.1	−0.4	0.1	−0.5	0.5
2014/2015	0.2	0.1	+0.0	0.0	0.4	0.1	0.2	0.3
2015/2016	−1.3	0.6	−0.8	0.2	−1.3	0.4	−1.1	0.5

Note. Calibrated Σ_{SMB} estimates are summarized in an ensemble mean including spread (max-min). Units are 10^{12} kg/a, that is, Gt/a. SMB = surface mass balance.

approaches to estimate RCM ELA uncertainty. Uncertainty in ELA estimated from field data is based on the SMB ablation area regression parameters described in section 3.3. In 2013/2014–2015/2016, ELA uncertainty was +12% and −11% on average. We added another 50% to this uncertainty, that is, +19% and −16%, in other balance years, where number of SMB observations was too low to estimate regression parameter uncertainty.

We suggest the most reliable RCM ELA values to be those with the highest correlation with the field data. For example, HIRHAM5 represents the Q-transect with relatively few (13) grid elevations, only 4 of which are below 1,000 m (grid locations at 289, 571, 757, and 957 m). In years of ELA < 757 m, Linfit and VanDeWal method uses only two grid points resulting in an estimate having a low correlation with field data. The Interp ELA estimated from HIRHAM5 yielded values of $1,169 \pm 278$ m over the 2000/2001–2002/2003 and 2007/2008–2015/2016 period, hereafter "observational period," having a $R^2 = 0.74$ with ELA estimated from Q-transect observations (observational period average of $1,039 \pm 98$ m). For MAR, the Interp and Linfit methods show equally high correlation ($R^2 = 0.74$) with observations. The annual average of the two methods resulted in better agreement with observations ($R^2 = 0.75$) and average ELA = $1,260 \pm 120$ m over the observational period. Interannual standard deviation (σ) is more than 2 times smaller. The best estimate of ELA from RACMO2 comes from the annual average of all three methods ($R^2 = 0.60$ with observations) and ensemble ELA = 930 ± 236 m.

On average, the MAR and HIRHAM5 ELAs are significantly different (respectively: 221 and 130 m, higher) than the observations. The RACMO2 ELA estimates are significantly (109 m) lower than the observations. Significance is here ascribed when the RCM differences exceed 1σ of the observational data (whiskers to the right in Figure 9). The better ELA agreement of HIRHAM5 and RACMO2 is related to the findings discussed in section 3.4, that between −0.5- and +0.3-mWE SMB, we find satisfactory agreement between HIRHAM5 and the Q-transect field data (Figure 6). RACMO2 ELA is also closer to the observational ELAs. Even though the MAR offset to field data is largest, MAR shows a similar magnitude of temporal variability and highest correlation with Q-transect observations among the three RCMs ($R^2 = 0.74$).

While, HIRHAM5 and MAR ELA values suggest an increasing ELA over time, RACMO2 and the smaller sample of observation estimated ELA do not suggest a significant ELA increase.

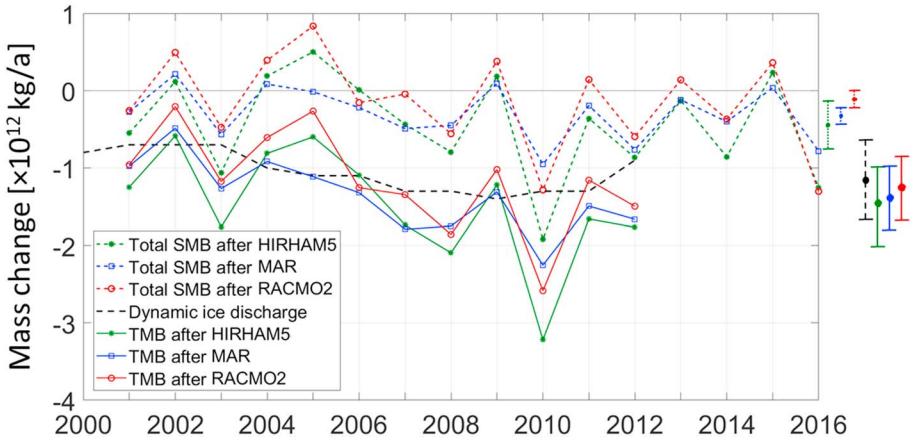

Figure 10. Total HIRHAM5, MAR, and RACMO2 SMB from 2000/2001–2015/2016 and D from 2000 to 2012 (Enderlin et al., 2014), summing up to the TMB in 2000/2001–2011/2012. Average mass flux and absolute uncertainty values are indicated using whiskers to the right of the graphic. SMB = surface mass balance; TMB = total mass balance.

3.6. Sermilik Glacier SMB and TMB

We finally evaluate the importance of a precise SMB simulation for catchment area-integrated SMB (hereafter Σ_{SMB}) and total mass balance (hereafter TMB, with TMB = Σ_{SMB} − ice flow discharge [D]). We estimate Σ_{SMB} using HIRHAM5, MAR, and RACMO2 cumulative SMB over hydrological years (1 October to 31 September), each calibrated with the Q-transect ablation area SMB observations for the Sermilik catchment area delineated from the Sentinel-1-derived velocity map after Nagler et al. (2015, section 2.4). We assume that HIRHAM5 SMB more positive than −0.5 mWE are accurate given their agreement with the field data (Figure 6). The inverse function of the regression in Figure 6, $x = (y + 0.27)/0.45$ [mWE], was used to calibrate HIRHAM5 SMB output below SMB = −0.5 mWE, where we found a large HIRHAM5 bias. Calibration to MAR and RACMO2 was applied to all SMB points below highest elevation where negative SMB was simulated with the functions: $x = (y + 0.92)/0.73$ and $x = (y - 0.55)/0.55$ [mWE], respectively. Due to lacking accumulation observations above ELA in the Sermilik catchment, we do not calibrate accumulation rates above ELA. Since SMB is calibrated among the models in the ablation area, the driver of disagreement among RCM averaged Σ_{SMB} above ELA is accumulation uncertainty.

The uncertainty of SMB in each RCM is here taken as 1σ of the postcalibration residuals, equal to 45% (HIRHAM5), 23% (MAR), or 31% (RACMO2) of the mean SMB on the ensemble average, see Figures 6b, 6d, and 6f in section 3.2. The result was a SMB elevation profile for years 2000/2001–2015/2016 subsequently integrated over Sermilik glacier elevation span, accounting for the area variation of each elevation range, that is, the hypsometry.

Over the 2000/2001–2015/2016 period, Σ_{SMB} was positive in three balance years (2003/2004, 2008/2009, and 2014/2015). However, the three RCMs do not agree on the sign of Σ_{SMB} in four balance years (2004/2005, 2005/2006, 2010/2011, and 2012/2013; Table 7). Over 2000/2001–2011/2012, however, the multiyear Sermilik catchment Σ_{SMB} averages below 0 Gt/a after two RCMs (−0.4 ± 0.3 Gt/a [HIRHAM5] and −0.3 ± 0.1 Gt/a [MAR]). Multiyear averaged RACMO2 Σ_{SMB} was −0.1 ± 0.1 Gt/a. The three RCMs are summarized in an ensemble mean Σ_{SMB} suggesting an insignificant imbalance (−0.3 ± 0.3 Gt/a).

Given D for Sermilik glacier that averaged 1.1 ± 0.6 Gt/a during the 2001–2012 period (Enderlin et al., 2014) and the above calibrated ensemble Σ_{SMB}, we estimate the time series of TMB (Figure 10 and Table 8). We acknowledge that D was reported for calendar years and Σ_{SMB} is reported for the hydrological years. We assume that seasonal variability in D is small compared to interannual variability in D per Ahlstrøm et al. (2013) continuous Global Positioning System observations. We effectively match each hydrological year's Σ_{SMB} with a 3-month lagged calendar year D. We computed uncertainty in TMB as averaged uncertainty of Σ_{SMB} and D weighed by their contribution to TMB. The precision of our TMB results is reduced by the D values available from Enderlin et al. (2014) being limited to 0.1 Gt. Our Σ_{SMB} uncertainty is on that order of magnitude. The three RCM ensemble mean and spread (max-min), combined with the Enderlin et al. (2014) D data, suggest an average TMB of Sermilik glacier of −1.3 ± 0.5 Gt/a during the 2000/2001 to 2011/2012 12-year period. The ensemble mean TMB is most negative in 2009/2010 (−2.7 ± 0.9 Gt/a), and least negative during 2001/2002 (−0.4 ± 0.4 Gt/a).

Table 8
D Including an Average Absolute Uncertainty of 50% (Enderlin et al., 2014) and TMB Estimates of the Three RCMs

	Enderlin et al. (2014)		HH5		MAR		RACMO2		Ensemble	
Balance year	D	±	TMB	±	TMB	±	TMB	±	TMB	Spread
2000/2001	0.7	0.4	−1.2	0.3	−1.0	0.3	−1.0	0.3	−1.0	0.2
2001/2002	0.7	0.4	−0.6	0.3	−0.5	0.3	−0.2	0.3	−0.4	0.4
2002/2003	0.7	0.4	−1.8	0.4	−1.3	0.2	−1.2	0.2	−1.4	0.6
2003/2004	1.0	0.5	−0.8	0.4	−0.9	0.5	−0.6	0.4	−0.8	0.3
2004/2005	1.1	0.6	−0.6	0.4	−1.1	0.6	−0.3	0.4	−0.7	0.8
2005/2006	1.1	0.6	−1.1	0.6	−1.3	0.5	−1.3	0.5	−1.2	0.2
2006/2007	1.3	0.7	−1.7	0.5	−1.8	0.5	−1.3	0.7	−1.6	0.4
2007/2008	1.3	0.7	−2.1	0.6	−1.7	0.5	−1.9	0.5	−1.9	0.4
2008/2009	1.4	0.7	−1.2	0.6	−1.3	0.7	−1.0	0.6	−1.2	0.3
2009/2010	1.3	0.7	−3.2	0.8	−2.3	0.5	−2.6	0.5	−2.7	0.9
2010/2011	1.3	0.7	−1.7	0.5	−1.5	0.6	−1.2	0.6	−1.5	0.5
2011/2012	0.9	0.5	−1.8	0.4	−1.7	0.3	−1.5	0.4	−1.7	0.3
Average	1.1	0.5	−1.5	0.5	−1.4	0.4	−1.2	0.4	−1.3	0.5

Note. TMB uncertainty is weighed average uncertainty of calibrated Σ_{SMB} and D according to their contributions to TMB. RCM estimates are summarized in an ensemble including a spread (max-min). Units are Gt/a. TMB = total mass balance; RCM = regional climate model.

D accounted for 72% of the TMB ensemble mean magnitude on average. However, Σ_{SMB} is responsible for more of the loss in extreme mass loss years (e.g., 2002/2003 and 2009/2010), when it contributed 50% and 52%, respectively, to ensemble mean TMB. A less negative (or positive) Σ_{SMB} in turn made the TMB less negative than D. For instance, in the extreme surface mass loss year 2011/2012, TMB was less negative than in 2009/2010 due to a larger winter accumulation counteracting melt that year (see Fausto, van As, Box, Colgan, Langen, & Mottram, 2016).

Our estimated changes in Σ_{SMB}, D, and TMB for the Sermilik catchment contrast with the whole ice sheet changes reported by Van den Broeke et al. (2016) finding Σ_{SMB} and not D responsible for the majority of TMB. At the Sermilik glacier scale, interannual fluctuations in Σ_{SMB} are relatively large in comparison to interannual fluctuations in D. Nonetheless, D nearly doubled between 2003 and 2009, from 0.7 ± 0.5 to 1.4 ± 0.7 Gt/a, but by 2012 returned to 0.9 ± 0.5 Gt/a. During the 2000/2001–2011/2012 period, correlation of annual Σ_{SMB} with TMB ($R^2 = 0.81$) is significant while that of annual −D is not ($R^2 = 0.24$). The dominance of Σ_{SMB} on the TMB temporal variance suggests a strong role of SMB in modulating ice sheet mass loss, despite Sermilik being a tidewater ice sheet catchment and D being 3 times Σ_{SMB} in magnitude. The importance of SMB is prominent in south Greenland, where interannual variability in the competing fluxes of ice ablation and snow accumulation is pronounced.

The average of the TMB ensemble between 2000/2001 and 2011/2012 expressed as specific mass loss: 1.3 Gt/a distributed over the Sermilik catchment area (559 km^2) is equivalent to 2.3 mWE/a. Sermilik specific mass loss exceeds, for example, the average of Patagonia (the world's most rapidly depleting Randolph Glacier Inventory unit) of 1.8 mWE/a estimated by Kaser et al. (2006) over the 1990–2000 period. The Sermilik glacier, representative of the larger Qagssimiut ice lobe of the southern Greenland ice sheet, is therefore losing mass at a specific rate that is comparable to the loss rate from lower latitude glaciers.

The Sermilik catchment represents 0.03% of the total ice sheet area of 1.7×10^6 km^2. The average annual TMB of the Sermilik catchment during 2002/2003–2008/2009 period (ensemble mean of -1.3 ± 0.5 Gt/a), however, is equivalent to approximately 0.61% of mass loss from the ice sheet proper during the 2003–2009 period (Colgan et al., 2015). The mass loss of the Sermilik catchment, from peripheral tidewater margin to interior flow divide, is therefore disproportionately large (factor of $0.61/0.03 \approx 20$) in comparison to the Greenland ice sheet as whole. When contrasting Sermilik TMB to ice sheet TMB in 2007 and 2011 found by Andersen et al. (2015), we find similar factors of 19 and 17, respectively. Comparing at a smaller scale, namely, with flux gate section 5 in Southwest Greenland (Andersen et al., 2015), Sermilik glacier mass loss is six (2011) to eight (2007) times higher.

4. Conclusions

4.1. Q-Transect Observations

The updated set of southern Greenland ice sheet ablation area SMB data presented here spans 16 balance years beginning in 2000/2001. This PROMICE Qagssimiut ice lobe Q-transect now with nine locations surveyed since 2013 (across a 850-m elevation range) provides insight into spatiotemporal variability in net snow accumulation and ablation of the southern tip of the Greenland ice sheet.

The Q-transect field data indicate an orographic accumulation peak in the 800 to 900 m elevation range. The interannual variation in accumulation and ablation rates is up to 1 mWE, large as compared to other PROMICE field observation regions. Annual ablation at the QAS_L site varies by more than a factor of 2 between low and high ablation years. More than a factor of 2 extremes in SMB result from a combination of occasional heatwave conditions (periods of strong 5+ m/s daily average wind speed, high 5+ °C air temperature, and high 5+ g/kg humidity on-shore flow) and low or high snow cover totals.

The Q-transect ELA during 2000/2001 to 2016/2017 is $1,039 \pm 98$ m. There are, however, too few reliable years to deduce any signficant ELA trend from the observational record. Ablation gradients with elevation are higher than at other PROMICE regions in Greenland, indicative of high mass turnover interacting with ice flow in steepening the ice sheet elevation profile.

From 22 coincident observations, we find snow thickness over the Q-transect to be a strong predictor of SWE, consistent with Sturm et al. (2010). An empirical function based on the relationship is presented and used to extend the SWE records by six additional balance years.

4.2. RCM Validation

By comparison between the Q-transect field data and output from three RCMs (HIRHAM5 after Langen et al., 2015, 2017; MAR v3.7 after Fettweis et al., 2017; RACMO2.3p2 after Noël et al., 2018), we find that the MAR and HIRHAM5 RCM ELAs are significantly higher (respectively, 221 and 130 m) than the observations and the RACMO2 RCM ELA estimates are significantly lower (109 m) than the observations. While MAR indicates an increasing ELA over the study period, there is no trend in the HIRHAM5 and RACMO2.3p2 data.

The RCMs underestimate lower ablation area ice melt. A wet bias (too much snow accumulation) in HIRHAM5 and RACMO2 is likely the dominant error source. Yet the MAR RCM also underestimates ice melt in the lower ablation area while simulating accumulation with no wet bias below ELA. Overestimation of bare ice albedo because of background impurities that are not parameterized is likely the cause of the too small melt bias in MAR. HIRHAM5 and RACMO2 account for (dark) background impurities. Another source of bias for all RCMs likely involves underestimation of downward turbulent heat fluxes that appear to be not fully resolved by the bulk method.

Per Fausto, van As, Box, Colgan, and Langen (2016) and Fausto, van As, Box, Colgan, Langen, and Mottram (2016), we posit that the bulk method used by RCMs and applied to PROMICE station data underestimates downward turbulent energy flux, at least during heatwaves (as described in section 4.1), leading to the recommendatoin of using fast-responding ultrasonic anemometers and hygrometers to pinpoint inaccuracies with the turbulent heat flux estimates from average wind speed, temperature, and humidity (aka "profile") data. With turbulence sensors, we may better estimate z_0, vertical gradients and stability correction functions to better represent vertical turbulent transfer under a range of circumstances. Only then may we more fully diagnose RCM biases in turbulent heat transfer and in turn SMB biases.

4.3. Sermilik Glacier SMB and TMB

Calibrating the three RCMs using the Q-transect field data for the catchment area defined by the Sentinel-1 velocity map enabled closing of the SMB and TMB of the Sermilik glacier with much more precision and accuracy than possible earlier. With annual estimates spanning 2000/2001 to 2011/2012, we compute an average SMB of the Sermilik glacier catchment to be -0.3 ± 0.5 and TMB of -1.3 ± 0.5 Gt/a. Dynamic ice discharge constitutes 72% of TMB. Only in the two extreme surface mass loss years (2002/2003 and 2009/2010) did SMB contribute more mass loss than ice flow discharge. The temporal variability in TMB is better explained by that in SMB than of ice flow discharge (D), though the temporal variability in D may be larger if sampled more than once per year.

Given high accumulation and ablation rates captured by the Q-transect, the location is well placed to monitor a glacier in a high mass turnover sub-Arctic region. Sermilik specific mass loss exceeds, for example, the average of Patagonia (the world's most rapidly depleting Randolph Glacier Inventory unit) of 1.8 mWE/a estimated by Kaser et al. (2006) over the 1990–2000 period. The Sermilik glacier, representative of the larger Qagssimiut ice lobe of the southern Greenland ice sheet, is therefore losing mass at a specific rate that is comparable to lower latitude glaciers.

When contrasting Sermilik catchment TMB to that of the whole ice sheet, its specific TMB (TMB divided by the catchment area) is 20 times that of the Greenland ice sheet averaged over the period 2003 to 2009 (Colgan et al., 2015). In years 2007 and 2011, we find similar ratios of 19 and 17 (Andersen et al., 2015), respectively, suggesting that the Sermilik glacier catchment is an ice mass loss hot spot.

Acknowledgments
This study is funded by DANCEA (Danish Cooperation for Environment in the Arctic) under the Danish Ministry of Energy, Buildings and Climate through the Programme for Monitoring of the Greenland Ice Sheet (PROMICE) and by the Independent Research Fund Denmark grant 4002-00234. Mauro Hermann visiting GEUS for 5 months was supported by a grant from the Excellence Scholarship and Opportunity Programme (ESOP) from Eidgenössische Technische Hochschule (ETH) Zürich. Intellectual and practical support for 2017 fieldwork came from Matthias Jaggi and Martin Schneebeli from the WSL Institut für Schnee und Lawinenforschung (SLF), Davos Switzerland. The stake networks Q1 to Q6 were initiated in September 2013 with financial support from Vice.com. The work was developed under the framework of the Network on Arctic Glaciology of the International Arctic Science Committee (IASC-NAG). Brice Noël and Michiel van den Broeke acknowledge support from the Netherlands Earth System Science Centre (NESSC). We declare no real or perceived financial conflicts of interests for any of the authors. Much of the field data used here are listed in tables and supporting information and can be provided upon request through http://promice.dk. PROMICE station data are available from http://promice.dk/WeatherArchive.html. We thank Þorsteinn Þorsteinsson of the Icelandic Met Office for providing comments on the manuscript. We thank Xavier Fettweis for sharing MAR output and providing constructive input as an external reviewer.

References

Ahlstrøm, A., Andersen, S. B., Nick, F. M., Reijmer, C. H., van de Wal, R. S. W., & Hubbard, A. (2013). Seasonal velocities of eight major marine-terminating outlet glaciers of the Greenland ice sheet from continuous in situ GPS instruments. *Earth system science data discussions*, *6*(1), 27–57.

Ahlstrøm, A. P., Gravesen, P., Andersen, S. B., van As, D., Citterio, M., Fausto, R. S., & Stenseng, L. (2008). *A new programme for monitoring the mass loss of the Greenland Ice Sheet*. Copenhagen: Denmark.

Andersen, M. L., Stenseng, L., Skourup, H., Colgan, W., Khan, S. A., Kristensen, S. S., & Forsberg, R. (2015). Basin-scale partitioning of Greenland ice sheet mass balance components (2007–2011). *Earth and Planetary Science Letters*, *409*, 89–95.

Andreas, E. L. (1987). A theory for the scalar roughness and the scalar transfer coefficients over snow and sea ice. *Boundary-Layer Meteorology*, *38*, 159–184.

Andreas, E. L. (2002). Parameterizing scalar transfer over snow and ice: A review. *Journal of Hydrometeorology*, *3*, 417–432.

Bøggild, C. E., & Podlech, S. (2006). Significant thinning of the south Greenland Ice Sheet margin. *Weather*, *61*(4), 102–105.

Box, J. E., Bromwich, D. H., & Bai, L.-S. (2004). Greenland ice sheet surface mass balance for 1991–2000: Application of Polar MM5 mesoscale model and in-situ data. *Journal of Geophysical Research*, *109*, D16105. https://doi.org/10.1029/2003JD004451

Box, J. E., & Colgan, W. (2013). Greenland ice sheet mass balance reconstruction. Part III: Marine ice loss and total mass balance (1840–2010). *Journal of Climate*, *26*, 6990–7002. https://doi.org/10.1175/ JCLI-D-12-00546.1

Box, J. E., Cressie, N., Bromwich, D. H., Jung, J., van den Broeke, M., van Angelen, J. H., et al. (2013). Greenland ice sheet mass balance reconstruction. Part I: Net snow accumulation (1600–2009). *Journal of Climate*, *26*, 3919–3934.

Box, J. E., Fettweis, X., Stroeve, J. C., Tedesco, M., Hall, D. K., & Steffen, K. (2012). Greenland ice she et albedo feedback: Thermodynamics and atmospheric drivers. *The Cryosphere*, *6*(4), 821–839.

Box, J. E., & Steffen, K. (2001). Sublimation estimates for the Greenland ice sheet using automated weather station observations. *Journal of Geophysical Research*, *106*(D24), 33,965–33,982.

Box, J. E., van As, D., & Steffen, K. (2017). Greenland, Canadian and Icelandic land ice albedo grids (2000–2016). *Geological Survey of Denmark and Greenland Bulletin*, *38*, 69–72.

Braithwaite, R. J. (1984). Short notes: Can the mass balance of a glacier be estimated from its equilibrium-line altitude? *Journal of Glaciology*, *30*(106), 364–368.

Brock, B. W., Willis, I. C., & Shaw, M. J. (2006). Measurement and parameterization of aerodynamic roughness length variations at Haut Glacier d'Arolla, Switzerland. *Journal of Glaciology*, *52*, 281–297.

Brun, E., David, P., Sudul, M., & Brunot, G. (1992). A numerical model to simulate snowcover stratigraphy for operational avalanche forecasting. *Journal of Glaciology*, *38*, 13–22.

Burgess, E. W., Forster, R. R., Box, J. E., Mosley-Thompson, E., Bromwich, D. H., Bales, R. C., & Smith, L. C. (2010). A spatially calibrated model of annual accumulation rate on the Greenland Ice Sheet (1958–2007). *Journal of Geophysical Research*, *115*, F02004. https://doi.org/10.1029/2009JF001293

Charalampidis, C., van As, D., Langen, P. L., Fausto, R. S., Vandecrux, B., & Box, J. E. (2016). Regional climate-model performance in Greenland firn derived from in-situ observations. *Geological Survey of Denmark and Greenland Bulletin*, *35*, 75–78.

Christensen, O. B., Drews, M., Christensen, J. H., Dethloff, K., Ketelsen, K., Hebestadt, I., & Rinke, A. (2007). The HIRHAM5 regional climate model (*Technical Report No. 06-17*). Copenhagen: Version 5, Danish Meteorological Institute. available at dmi.dk.

Colgan, W., Abdalati, W., Citterio, M., Csatho, B., Fettweis, X., Luthcke, S., & Stober, M. (2015). Hybrid glacier Inventory, Gravimetry and Altimetry (HIGA) mass balance product for Greenland and the Canadian Arctic. *Remote Sensing of Environment*, *168*, 24–39.

Dee, D. P., Uppala, S., Simmons, A., Berrisford, P., Poli, P., Kobayashi, S., et al. (2011). The ERA-Interim reanalysis: Configuration and performance of the data assimilation system. *Quarterly Journal of the Royal Meteorological Society*, *137*, 553–597.

Drusch, M., Del Bello, U., Carlier, S., Colin, O., Fernandez, V., Gascon, F., & Meygret, A. (2012). Sentinel-2: ESA's optical high-resolution mission for GMES operational services. *Remote Sensing of Environment*, *120*, 25–36.

ECMWF-IFS (2008). Part IV: Physical processes (CY33R1) (Technical Report). Shinfield Park, Reading, UK: European Center for Medium-Range Weather Forecasts.

Enderlin, E. M., Howat, I. M., Jeong, S., Noh, M. J., Angelen, J. H., & Broeke, M. R. (2014). An improved mass budget for the Greenland ice sheet. *Geophysical Research Letters*, *41*, 866–872. https://doi.org/10.1002/2013GL059010

Ettema, J., van den Broeke, M. R., van Meijgaard, E., & van de Berg, W. J. (2010). Climate of the Greenland ice sheet using a high-resolution climate model—Part2: Near-surface climate and energy balance. *The Cryosphere*, *4*, 529–544. https://doi.org/10.5194/tc-4-529-2010

Ettema, J., van den Broeke, M. R., van Meijgaard, E., van de Berg, W. J., Bamber, J. L., Box, J. E., & Bales, R. C. (2009). Higher surface mass balance of the Greenland ice sheet revealed by high-resolution climate modeling. *Geophysical Research Letters*, *36*, L12501. https://doi.org/10.1029/2009GL038110

Fausto, R. S., van As, D., Box, J. E., Colgan, W., Langen, P. L., & Mottram, R. H. (2016). The implication of nonradiative energy fluxes dominating Greenland ice sheet exceptional ablation area surface melt in 2012. *Geophysical Research Letters*, *43*, 2649–2658. https://doi.org/10.1002/2016GL067720

Fausto, R. S., van As, D., Ahlstrøm, A. P., Andersen, S. B., Andersen, M. L., Citterio, M., & Weidick, A. (2012). Ablation observations for 2008–2011 from the Programme for Monitoring of the Greenland Ice Sheet (PROMICE). *Geological Survey of Denmark and Greenland Bulletin*, *26*, 73–76.

Fausto, R. S., van As, D., Ahlstrøm, A. P., & Citterio, M. (2012). Assessing the accuracy of Greenland ice sheet surface ablation measurements by pressure transducer. *Journal of Glaciology*, *58*(212), 1144–1150. https://doi.org/10.3189/2012JoG12J075

Fausto, R. S., van As, D., Box, J. E., Colgan, W., & Langen, P. L. (2016). Quantifying the surface energy fluxes in south Greenland during the 2012 high melt episodes using in-situ observations. *Frontiers in Earth Science*, *4*, 82.

Fausto, R. S., van As, D. & PROMICE Project Team (2012). Ablation observations for 2008–2011 from the Programme for Monitoring of the Greenland Ice Sheet (PROMICE). *Geological Survey of Denmark and Greenland Bulletin*, *26*, 73–76.

Fettweis, X. (2007). Reconstruction of the 1979–2006 Greenland ice sheet surface mass balance using the regional climate model MAR. *The Cryosphere*, *1*, 21–40. https://doi.org/10.5194/tc-1-21-2007

Fettweis, X., Box, J. E., Agosta, C., Amory, C., Kittel, C., Lang, C., et al. (2017). Reconstructions of the 1900–2015 Greenland ice sheet surface mass balance using the regional climate MAR model. *The Cryosphere*, *11*, 1015–1033. https://doi.org/10.5194/tc-11-1015-2017

Fettweis, X., Gallée, H., Lefebre, L., & van Ypersele, J.-P. (2005). Greenland surface mass balance simulated by a regional climate model and comparison with satellite derived data in 1990–1991. *Climate Dynamics*, *24*, 623–640. https://doi.org/10.1007/s00382-005-0010-y

Fettweis, X., Hanna, E., Lang, C., Belleflamme, A., Erpicum, M., & Gallée, H. (2013). Brief communication "Important role of the mid-tropospheric atmospheric circulation in the recent surface melt increase over the Greenland ice sheet". *The Cryosphere*, *7*(1), 241–248.

Galleé, H., Guyomarch, G., & Brun, E. (2001). Impact of the snow drift on the Antarctic ice sheet surface mass balance: possible sensitivity to snow-surface properties. *Boundary-Layer Meteorology*, *99*, 1–19.

Gallée, H., & Schayes, G. (1994). Development of a three-dimensional meso-γ primitive equations model. *Monthly Weather Review*, *122*, 671–685.

Kaser, G., Cogley, J. G., Dyurgerov, M. B., Meier, M. F., & Ohmura, A. (2006). Mass balance of glaciers and ice caps: Consensus estimates for 1961–2004. *Geophysical Research Letters*, *33*, L19501. https://doi.org/10.1029/2006GL027511

Kjeldsen, K. K., Korsgaard, N. J., Bjørk, A. A., Khan, S. A., Funder, S., Larsen, N. K., & Nuth, C. (2015). Spatial and temporal distribution of mass loss from the Greenland Ice Sheet since AD 1900. *Nature*, *528*(7582), 396–400.

Kuipers Munneke, P., van den Broeke, M. R., Lenaerts, J. T. M., Flanner, M. G., Gardner, A. S., & van de Berg, W. J. (2011). A new albedo parameterization for use in climate models over the Antarctic ice sheet. *Journal of Geophysical Research*, *116*, D05114. https://doi.org/10.1029/2010JD015113

Langen, P. L., Fausto, R. S., Vandecrux, B., Mottram, R. H., & Box, J. E. (2017). Liquid water flow and retention on the Greenland Ice Sheet in the regional climate model HIRHAM5: Local and large-scale impacts. *Frontiers in Earth Science*, *4*, 110.

Langen, P. L., Mottram, R. H., Christensen, J. H., Boberg, F., Rodehacke, C. B., Stendel, M., & Petersen, D. (2015). Quantifying energy and mass fluxes controlling Godthåbsfjord freshwater input in a 5-km simulation (1991–2012). *Journal of Climate*, *28*(9), 3694–3713.

Larsen, N. K., Kjr, K. H., Lecavalier, B., Bjørk, A. A., Colding, S., Huybrechts, P., & Olsen, J. (2015). The response of the southern Greenland ice sheet to the Holocene thermal maximum. *Geology*, *43*(4), 291–294.

Lecavalier, B. S., Milne, G. A., Simpson, M. J., Wake, L., Huybrechts, P., Tarasov, L., & Dyke, A. S. (2014). A model of Greenland ice sheet deglaciation constrained by observations of relative sea level and ice extent. *Quaternary Science Reviews*, *102*, 54–84.

Lenaerts, J. T. M., van den Broeke, M. R., Angelen, J. H., van Meijgaard, E., & Dery, S. J. (2012). Drifting snow climate of the Greenland ice sheet: A study with a regional climate model. *The Cryosphere*, *6*, 891–899. https://doi.org/10.5194/tc-6-891-2012

Ligtenberg, S. R. M., Helsen, M. M., & van den Broeke, M. R. (2011). An improved semi-empirical model for the densification of Antarctic firn. *The Cryosphere*, *5*, 809–819. https://doi.org/10.5194/ tc-5-809-2011

Lindbäck, K., Pettersson, R., Hubbard, A. L., Doyle, S. H., As, D., Mikkelsen, A. B., & Fitzpatrick, A. A. (2015). Subglacial water drainage, storage, and piracy beneath the Greenland ice sheet. *Geophysical Research Letters*, *42*, 7606–7614. https://doi.org/10.1002/2015GL065393

Lucas-Picher, P., Wulff-Nielsen, M., Christensen, J. H., Aoalgeirsdóttir, G., Mottram, R., & Simonsen, S. B. (2012). Very high resolution regional climate model simulations over Greenland: Identifying added value. *Journal of Geophysical Research*, *117*, D02108. https://doi.org/10.1029/2011JD016267

Machguth, H., Thomsen, H. H., Weidick, A., Ahlstrøm, A. P., Abermann, J., Andersen, M. L., et al. (2016). Greenland surface mass-balance observations from the ice-sheet ablation area and local glaciers. *Journal of Glaciology*, *62*, 861–887.

McConnell, J. R., Mosley-Thompson, E., Bromwich, D. H., Bales, R. C., & Kyne, J. D. (2000). Interannual variations of snow accumulation on the Greenland Ice Sheet (1985–1996): New observations versus model predictions. *Journal of Geophysical Research*, *105*(D3), 4039–4046.

Mernild, S. H., Hanna, E., McConnell, J. R., Sigl, M., Beckerman, A. P., Yde, J. C., et al. (2015). Greenland precipitation trends in a long-term instrumental climate context (1890–2012): Evaluation of coastal and ice core records. *International Journal of Climatology*, *35*, 303–320. https://doi.org/10.1002/joc.3986

Mernild, S. H., & Liston, G. E. (2010). The influence of air temperature inversion on snow melt and glacier surface mass-balance simulations, SW Ammassalik Island, SE Greenland. *Journal of Applied Meteorology and Climatology*, *49*(1), 47–67.

Miège, C., Forster, R. R., Box, J. E., Burgess, E. W., McConnell, J. R., Pasteris, D. R., & Spikes, V. B. (2013). Southeast Greenland high accumulation rates derived from firn cores and ground-penetrating radar. *Annals of Glaciology*, *54*(63), 322–332.

Morin, P., Porter, C., Cloutier, M., Howat, I., Noh, M. J., Willis, M., et al. (2016). ArcticDEM: A publically available, high resolution elevation model of the Arctic. *EGU General Assembly 2016, held 17-22 April, 2016 in Vienna Austria, id. EPSC2016-8396*.

Nagler, T., Rott, H., Hetzenecker, M., Wuite, J., & Potin, P. (2015). The Sentinel-1 mission: New opportunities for ice sheet observations. *Remote Sensing*, *7*, 9371–9389.

Neff, W., Compo, G. P., Martin Ralph, F., & Shupe, M. D. (2014). Continental heat anomalies and the extreme melting of the Greenland ice surface in 2012 and 1889. *Journal of Geophysical Research: Atmospheres*, *119*, 6520–6536. https://doi.org/10.1002/2014JD021470

Niwano, M., Aoki, T., Matoba, S., Yamaguchi, S., Tanikawa, T., Kuchiki, K., & Motoyama, H. (2015). Numerical simulation of extreme snowmelt observed at the SIGMA-A site, northwest Greenland, during summer 2012. *The Cryosphere*, *9*, 971–988. https://doi.org/10.5194/tc-9-971-2015

Noël, B., van de Berg, W. J., Lhermitte, S., Wouters, B., Machguth, H., Howat, I., et al. (2017). A tipping point in refreezing accelerates mass loss of Greenland's glaciers and ice caps. *Nature Communications*, *8*, 14730.

Noël, B., van de Berg, W. J., Machguth, H., Lhermitte, S., Howat, I., Fettweis, X., & van den Broeke, M. R. (2016). A daily, 1 km resolution data set of downscaled Greenland ice sheet surface mass balance (1958–2015). *The Cryosphere*, *10*(5), 2361–2377.

Noël, B., van de Berg, W. J., van Wessem, J. M., van Meijgaard, E., van As, D., Lenaerts, J. T. M., et al. (2018). Modelling the climate and surface mass balance of polar ice sheets using RACMO2—Part 1: Greenland (1958–2016). *The Cryosphere*, *12*, 811–831. https://doi.org/10.5194/tc-12-811-2018

Nordeng, T. E. (1994). Extended versions of the convective parameterization scheme at ECMWF and their impact on the mean and transient activity of the model in the tropics (Tech. Memo. 206). Reading, UK: Eur Centre for Medium-Range Weather Forecasts. Retrieved from https://www.ecmwf.int/en/elibrary/ 11393-extended-versions-convective-parametrization-scheme-ecmwf-and-their-impact-mean

Ohmura, A. (1987). New temperature distribution maps for Greenland. *Zeitschrift fur Gletscherkunde und Glaziolgeologie*, *23*, 1–45.

Ohmura, A., Calanca, P., Wild, M., & Anklin, M. (1999). Precipitation, accumulation and mass balance of the Greenland ice sheet. With 5 figures. *Zeitschrift fur Gletscherkunde und Glazialgeologie*, *35*(1), 1–20.

Ohmura, A., & Reeh, N. (1991). New precipitation and accumulation maps for Greenland. *Journal of Glaciology*, *37*(125), 140–148.

Podlech, S., Mayer, C., & Bøggild, C. E. (2004). Glacier retreat, mass-balance and thinning: Sermilik glacier, South Greenland. *Geografiska Annaler*, *86A*, 305–317.

Rae, J. G. L., Aalgeirsdóttir, G., Edwards, T. L., Fettweis, X., Gregory, J. M., Hewitt, H. T., et al. (2012). Greenland ice sheet surface mass balance: Evaluating simulations and making projections with regional climate models. *The Cryosphere*, *6*, 1275–1294. https://doi.org/10.5194/tc-6-1275-2012

Rignot, E., Box, J. E., Burgess, E., & Hanna, E. (2008). Mass balance of the Greenland ice sheet from 1958 to 2007. *Geophys Research Letters*, *35*, L20502. https://doi.org/10.1029/2008GL035417

Roeckner, E., Bäuml, G., Bonaventura, L., Brokopf, R., Esch, M., Giorgetta, M., et al. (2003). The atmospheric general circulation model ECHAM5. Part 1. Model description (Report no. 349). Max-Planck-Institut für Meteorologie (MPI-M).

Schmidt, L. S., Aoalgeirsdóttir, G., Gumundsson, S., Langen, P. L., Pálsson, F., Mottram, R., et al. (2017). The importance of accurate glacier albedo for estimates of surface mass balance on Vatnajökull: Evaluating the surface energy budget in a Regional Climate Model with automatic weather station observations. *The Cryosphere*, *11*, 1665–1684.

Smeets, C. J. P. P., & Van den Broeke, M. R. (2008a). The parameterisation of scalar transfer over rough ice. *Boundary-Layer Meteorology*, *128*(3), 339–355.

Smeets, C. J. P. P., & Van den Broeke, M. R. (2008b). Temporal and spatial variation of momentum roughness length in the ablation zone of the Greenland ice sheet. *Boundary-Layer Meteorology*, *128*, 315–338.

Studinger, M., Koenig, L., Martin, S., & Sonntag, J. (2010). Operation IceBridge: Using instrumented aircraft to bridge the observational gap between ICESat and ICESat-2. In *2010 IEEE International, Geoscience and Remote Sensing Symposium (IGARSS)* (pp. 1918–1919). Honolulu, HI: IEEE.

Sturm, M., Tareas, B., Liston, G. E., Derksen, C., Jonas, T., & Lea, J. (2010). Estimating snow water equivalent using snow depth data and climate classes. *Journal of Hydrometeorology*, *11*, 1380–1394.

Tedesco, M., Fettweis, X., Mote, T., Wahr, J., Alexander, P., Box, J. E., & Wouters, B. (2013). Evidence and analysis of 2012 Greenland records from spaceborne observations, a regional climate model and reanalysis data. *The Cryosphere*, *7*(2), 615–630.

Tedesco, M., Mote, T., Fettweis, X., Hanna, E., Jeyaratnam, J., Booth, J. F., et al. (2016). Arctic cut-off high drives the poleward shift of a new Greenland melting record. *Nature Communications*, *7*, 11723.

Tiedtke, M. (1989). A comprehensive mass flux scheme for cumulus parameterization in large-scale models. *Monthly Weather Review*, *117*(8), 1779–1800.

Undén, P., Rontu, L., Järvinen, H., Lynch, P., Calvo, J., Cats, G., et al. (2002). HIRLAM-5 scientific documentation (Scientific Report). Norrkoping, Sweden: Sveriges meteorologiska och hydrologiska institut. Can be downloaded from, http://hirlam.org

Van As, D., Andersen, M. L., Petersen, D., Fettweis, X., Van Angelen, J. H., Lenaerts, J., et al. (2014). Increasing meltwater discharge from the Nuuk region of the Greenland ice sheet and implications for mass balance (1960–2012). *Journal of Glaciology*, *60*(220), 314–322.

Van As, D., Bøggild, C. E., Nielsen, S., Ahlstrøm, A. P., Fausto, R. S., Podlech, S., & Andersen, M. L. (2009). Climatology and ablation at the South Greenland ice sheet margin from automatic weather station observations. *The Cryosphere Discussions*, *3*(1), 117–158.

Van As, D., Fausto, R. S., Colgan, W. T., Box, J. E., Ahlstrøm, A. P., Andersen, S. B., et al. (2013). Darkening of the Greenland ice sheet due to the melt-albedo feedback observed at PROMICE weather stations. *Geological Survey of Denmark and Greenland Bulletin*, *28*, 69–72.

Van As, D., Hubbard, A. L., Hasholt, B., Mikkelsen, A. B., Van den Broeke, M. R., & Fausto, R. S. (2012). Large surface meltwater discharge from the Kangerlussuaq sector of the Greenland ice sheet during the record-warm year 2010 explained by detailed energy balance observations. *Cryosphere*, *6*, 199–209. https: //doi.org/10.5194/tc-6-199-2012

Van Meijgaard, E., van Ulft, L. H., van de Berg, W. J., Bosveld, F. C., van den Hurk, B., Lenderink, G., & Siebesma, A. P. (2008). *Technical report 302: The KNMI regional atmospheric climate model RACMO version 2.1*. De Bilt: Royal Netherlands Meteorological Institute.

Van Wessem, J. M., Reijmer, C. H., Van de Berg, W. J., Van den Broeke, M. R., Cook, A. J., Van Ulft, L. H., & Van Meijgaard, E. (2015). Temperature and wind climate of the Antarctic Peninsula as simulated by a high-resolution regional atmospheric climate model. *Journal of Climate*, *28*, 7306–7326. https: //doi.org/10.1175/JCLI-D- 15-0060.1

Van de Berg, W. J., & Medley, B. (2016). Brief Communication: Upper-air relaxation in RACMO significantly improves modelled interannual surface mass balance variability in Antarctica. *The Cryosphere*, *10*, 459–463. https: //doi.org/10.5194/tc-10-459-2016

Van de Wal, R. S. W., Boot, W., Smeets, C. J. P. P., Snellen, H., van den Broeke, M. R., & Oerlemans, J. (2012). Twenty-one years of mass balance observations along the K-transect, West Greenland. *Earth System Science Data*, *4*, 31–35.

Van den Broeke, M. R., Enderlin, E. M., Howat, I. M., Kuipers Munneke, P., Noël, B. P. Y., van de Berg, W. J., et al. (2016). On the recent contribution of the Greenland ice sheet to sea level change. *The Cryosphere*, *10*, 1933–1946. https://doi.org/10.5194/tc-10-1933-2016

Vernon, C. L., Bamber, J. L., Box, J. E., van den Broeke, M. R., Fettweis, X., Hanna, E., & Huybrechts, P. (2013). Surface mass balance model intercomparison for the Greenland ice sheet. *The Cryosphere*, *7*, 599–614.

Winsor, K., Carlson, A. E., Caffee, M. W., & Rood, D. H. (2015). Rapid last-deglacial thinning and retreat of the marine-terminating southwestern Greenland ice sheet. *Earth and Planetary Science Letters*, *426*, 1–12.